3D auxetic mechanical metamaterials: an analytical, numerical, and experimental study

N. Ghavidelnia[1], M. Bodaghi[2], R. Hedayati[3,*]

[1]*Department of Mechanical Engineering, Amirkabir University of Technology (Tehran Polytechnic), Hafez Ave, Tehran, Iran*

[2]*Department of Engineering, School of Science and Technology, Nottingham Trent University, Nottingham NG11 8NS, United Kingdom*

[3]*Novel Aerospace Materials Group, Faculty of Aerospace Engineering, Delft University of Technology (TU Delft), Kluyverweg 1, 2629 HS Delft, the Netherlands*

---

[*] Corresponding author, email addresses: rezahedayati@gmail.com, r.hedayati@tudelft.nl, Tel: +31-15-2788777.

Abstract

Metamaterials are man-made rationally-designed structures that present unprecedented mechanical properties not found in nature. One of the most common metamaterials are Auxetics which demonstrate negative Poisson's ratio (NPR) behavior that is very beneficial for biomedical and engineering applications. In this study, a specific type of auxetic metamaterial structure namely idealized 3D re-entrant structure is studied analytically, numerically, and experimentally. The noted structure is constructed of three types of struts: one loaded purely axially, and two loaded simultaneously flexurally and axially which are inclined and are spatially defined by angles θ and φ). Analytical relationships for elastic modulus, yield stress, and Poisson's ratio of the 3D re-entrant unit cell based on two well-known beam theories namely Euler-Bernoulli and Timoshenko theories are derived. Moreover, two numerical approaches one based on beam elements and the other based on volumetric elements are implemented. Moreover, several specimens are additively manufactured and tested under compression. The analytical results had good agreement with volumetric numerical model and experimental results. Moreover, the effect of various geometrical parameters on the mechanical properties of the structure was studied and the results demonstrated that angle θ (related to tension-dominated struts) has the most effect on the sign of the Poisson's ratio and its extent, while angle φ (related to compression-dominated struts) has minimal effect on Poisson's ratio. However, the struts corresponding to φ angle provide strength and stiffness for the structure. The results also demonstrated that the structure could have zero Poison's ratio for a specific range of θ and φ angles. Finally, a lightened re-entrant structure is introduced and its results are compared to those of the idealized 3D re-entrant structure.

Keywords: Mechanical metamaterial, auxetics, negative Poisson's ratio, biomedical implants

1. Introduction

The Poisson's ratio of a material is defined as the ratio of negative value of transverse strain to the longitudinal strain of a body subjected to uniaxial stress [1]. The Poisson's ratio is usually assumed to be positive ($\nu > 0$) for natural materials which means that the material contracts transversely when stretched longitudinally or expands transversely when compressed longitudinally [2]. In contrast, there are some materials which reveal the opposite behaviour of common materials and present negative values for their Poisson's ratio which means that their transvers dimensions increase (or decrease) when they are subjected to axial tensile (or compressive) loads, respectively [3]. These materials have taken different names in the literature such as anti-rubber, dilational materials [4], and auxetic materials [5]. The term "auxetic" is currently widely accepted and used for the materials with negative Poisson's ratio. Auxetic behavior has been observed in a few natural materials such as Cristobalite (polymorphic silicones) [6], metals [7], zeolites [8], silicates [9, 10], as well as some biological tissues such as cancellous bone [11], tendons [12], and some animal skins [13, 14].

Mechanical metamaterials are man-made materials with unusual mechanical properties and special functionalities not found in nature [15-18]. Negative Poisson's ratio could be considered as one of such special mechanical properties [19]. Due to recent advances in additive manufacturing techniques (3D printing) which provides the possibility of fabrication of rationally-designed materials with desired accuracy in nano/micro scale [20, 21], the studies concentrated on design and analyzing auxetic metamaterials have been increasing during the last few years [22-25]. Different geometries for auxetic structures have been introduced with different deformation mechanisms. The re-entrant hexagonal honeycomb structure is one of the most well-known open cellular auxetic structure [26]. The effect of relative density and re-entrant angle variations on mechanical properties such as Poisson's ratio and elastic modulus of typical 2D re-entrant structure in elastic and plastic range have been analyzed for predicting the behavior of the structure in several studies [27-30]. To improve the mechanical properties of re-entrant structure such as strength and auxeticity as well as for new needs in industry, some researchers have introduced and build their 3D re-entrant structures inspired by typical 2D re-entrant unit cells and established analytical and numerical solutions for their auxetic structures [31-34].

The unit cell presented by Yang et al. (2015) is one of the successful auxetic structures which has been solved analytically in two directions and evaluated by experimental and numerical results [34] (Figure 1a). In another work, Wang et al. (2016) proposed an interlocking assembly manufacturing method for fabricating the same re-entrant lattice structure proposed by Yang et al. (2015) [34] but with a shifted unit cell (Figure 1b) which showed great advantages over additive manufacturing technique [35]. Chen et al. (2017) and Xue et al. (2020) applied some modifications to this 3D re-entrant auxetic structure by adding some struts to enhance the mechanical properties of the lattice structure, and in particular, to increase the stiffness of this auxetic structure [36, 37] (Figure 1c,d). Although the 3D reentrant structures studied in the noted works are successful auxetic structures for many applications, but they still lack some geometrical characteristics which could raise problems in many applications. First of all, even though the noted 3D re-entrant unit cells are symmetrical in the lateral directions, but their geometry is different in the vertical (i.e. loading) direction. Therefore, they exhibit dissimilar mechanical properties in the three main directions, which means that they are not truly 3D auxetic structures. Second, the struts at the edge of the noted unit cells are shared by adjacent unit cells in the lattice structure. Since the auxetic structures are applicable in many applications (such as implants, sandwich panels, etc.) which require graded micro-structures, the noted shared struts cause huge complexities and difficulties in creating a truly graded lattice structures. Hence, there remains a gap to propose an ideal unit cell which could overcome these deficiencies of typical 3D re-entrant structure.

In this study, a specific type of mechanical metamaterial structure namely idealized 3D re-entrant structure [38, 39] defined by three types of struts, one purely axially-loaded, and two simultaneously flexural- and axially-loaded (which are inclined and are spatially defined by angles θ and φ) is studied to obtain relationships for its mechanical properties (see Figure 2). Analytical solutions based on two well-known beam theories namely Euler-Bernoulli and Timoshenko theories are derived, and also two numerical methods with distinct elements types have been implemented for validating the results. A definition for strut effective length has been presented in order to simulate what the struts experience in real-life, and analytical results have been presented based on effective length. Moreover, a lightened auxetic unit cell extracted from the general re-entrant unit cell is presented and its mechanical properties are compared to those of the ideal re-entrant structure. Several specimens have also been additively manufactured and tested under compressive loading condition. Finally, the results of the derived analytical, constructed numerical models, and the manufactured specimens are compared to each other.

2. Materials and methods

2.1 Analytical solution

2.1.1 Relative density

Each re-entrant unit cell (Figure 2a) consists of three types of struts with lengths l_1, l_2, l_3 and cross-sectional areas A_1, A_2, A_3. The unit cell is fully defined with two unique angles θ and φ, the type-I strut length, and the main cube dimension (main cube is the hypothetical cube formed by connecting vertices D_i where $i = 1 \ to\ 8$). Angle θ is defined as the angle between type-II strut and the face diagonals of the main cube, and angle φ is defined as the angle between type-III strut and the sides of the main cube (Figure 2b). Each re-entrant unit cell with mentioned strut lengths (l_1, l_2, l_3) and characteristic angles (θ, φ) occupies a cubic volume with side length of $2(l_1 + l_3 \cos\varphi - l_2 \sin\theta)$ and thus the volume of $V_{total} = 8(l_1 + l_3 \cos\varphi - l_2 \sin\theta)^3$. Since the unit cell is made up of 6 struts of type I, 24 struts of type II, and 24 struts of type III, the volume occupied by the struts inside the unit cell is $V_{strut} = 6\pi r_1^2 l_1 + 24\pi r_2^2 l_2 + 24\pi r_3^2 l_3$. Therefore, according to the basic definition of relative density $\mu = \frac{V_{strut}}{V_{total}}$, the relative density of a re-entrant unit cell is given by

$$\mu = \frac{3\pi(r_1^2 l_1 + 4r_2^2 l_2 + 4r_3^2 l_3)}{4(l_1 + l_3 \cos\varphi - l_2 \sin\theta)^3} \tag{1}$$

2.1.2 Stiffness matrix

In this subsection, analytical relationships for mechanical properties of the 3D re-entrant unit cell such as elastic modulus, Poisson's ratio, and yield stress are derived as functions of elastic properties of matrix materials (E_s, G_s, σ_{ys}, and ν_s) and the geometrical dimensions of the unit cell. The re-entrant unit cell has symmetry with respect to its major planes, see Figure A1 in Appendix A. Therefore, studying 1/8 of the unit cell is sufficient for obtaining the mechanical properties of the unit cell and consequently the corresponding lattice structure. Because of the intrinsic symmetries in the geometry of re-entrant unit cell and the applied boundary conditions to the unit cell, seven unique group of vertices can be specified which are denoted by letters A, B, C, D, E, F and G, as shown in Figure 2a.

If the origin of the unit cell is considered in the midst of the unit cell, each re-entrant unit cell has four vertical (XY, YZ, and two bisectors of XY and YZ) and one horizontal (XZ) symmetry planes (as shown in Figure A1 in Appendix A). All the vertices located in the symmetry planes, are only allowed to translate and rotate in the corresponding planes. Vertices A_i and B_i (for i=1,2) are located in all four vertical symmetry planes, so they are only allowed to translate in the Y direction without any rotations. Therefore, they create two degrees of freedom (DOFs) q_8 and q_7 at vertices A_i and B_i, respectively. Vertices C_i (for $i = 1\ to\ 8$) are located in one vertical symmetry planes (XY or YZ), and they are only allowed to translate horizontally and vertically and rotate in their corresponding planes which results in three other DOFs (q_3, q_4, q_{11}). Each vertex D_i (for $i = 1\ to\ 8$) is located in a single vertical symmetry plane (one of two bisectors of YZ or YX), and therefore it is only allowed to translate horizontally and vertically and rotate in the planes it is located in, which leads to three other DOFs (q_5, q_6, q_{10}). Vertices E_i and F_i (for $i = 1\ to\ 4$) are located in one of two vertical symmetry planes (XY or YZ) and horizontal symmetry plane (XZ) so they are only allowed to translate in the X or Z directions without any rotations. This creates two other DOFs q_2 and q_1 at vertices E and F, respectively. Vertices G_i are located in horizontal symmetry plane (XZ) and in one of the vertical bisector symmetry planes (bisectors of XY or YZ). Therefore, these points cannot rotate in any directions and are only allowed to translate in the bisector of the noted planes which leads to the final DOF q_9. Overall, the system has a total number of 11 DOFs (Figure 2b).

In this study, two well-known elastic beam theories namely Euler-Bernoulli and Timoshenko beam theories have been implemented for analytical analysis of the re-entrant unit cell. As the beam theories and material models used for the analytical analysis are linear, the general deformation of the system can be considered as the sum of separate deformations caused by applying sole forces at each DOF. Therefore, the superposition principal could be used for obtaining the system of equations of the system. In this approach, each DOF displaces autonomously from other DOFs, and when a DOF is displaced, the other DOFs are kept fixed. By solving the equilibrium equations for the vertices of unit cell, the resultant forces could be obtained. By considering this method, the system of equilibrium equations for the structure could be written as $\{Q\} = [K]\{q\}$. In this equation, $\{Q\}$ is the force vector comprising the external forces acting on the DOFs, $[K]$ is the stiffness matrix of system, and the $\{q\}$ is the displacement vector.

As derivation of stiffness matrix elements are based on beam theories, the general deformation of a cantilever beam (Figure 3) can been considered as the resultant of four distinct deformations at the free end of the beam:

a) a lateral displacement without rotation, v
b) a flexural rotation without lateral displacement, θ
c) a longitudinal elongation or contraction, u
d) an axial twist, φ

The corresponding forces and moments required to create each of the pure mentioned deformations are demonstrated in Figure 4 for Euler-Bernoulli and Timoshenko beam theories. Due to frequent repetition of some terms demonstrated in Figure 4 throughout the whole manuscript, the terms S_i, W_i, T_i, V_i, and U_i are defined as new parameters and are listed in Table 1.

To explain the general procedure for derivation of stiffness matrix elements, we could assume a strut PQ with an arbitrary orientation with respect to global x, y and z coordinate system and having a unit vector of $\boldsymbol{u_{PQ}}$ which is affected by a specific DOF $\boldsymbol{q_i}$ at the free end of it. The schematic representation of such a strut and its deformation due to the DOF is shown in Figure 5. As it can be seen in the figure, DOF $\boldsymbol{q_i}$ causes a longitudinal and a transverse deformation in the strut PQ. The vector of longitudinal deformation of strut PQ can be obtained by projecting vector $\boldsymbol{q_i}$ on strut PQ, i.e.

$(\boldsymbol{q_i}.\boldsymbol{u}_{PQ})\boldsymbol{u}_{PQ}$, and the vector of transverse deformation of strut PQ can be calculated as $(\boldsymbol{q_i} - (\boldsymbol{q_i}.\boldsymbol{u}_{PQ})\boldsymbol{u}_{PQ})$. By multiplying the longitudinal deformation vector of strut PQ by the resultant force value of PQ (i.e. S_i), the resultant longitudinal force vector for strut PQ can be obtained as $\left((\boldsymbol{q_i}.\boldsymbol{u}_{PQ})\boldsymbol{u}_{PQ}\right)S_i$, and by multiplying the transverse deformation vector of strut PQ by the resultant transverse force value of PQ (i.e. T_i), the resultant transverse force vector for this strut can be obtained as $(\boldsymbol{q_i} - (\boldsymbol{q_i}.\boldsymbol{u}_{PQ})\boldsymbol{u}_{PQ})T_i$. The reaction moment vector, created by transverse deformation of strut PQ can be found by cross-product of unit vector of PQ (i.e. $\boldsymbol{u_{PQ}}$) and the resultant moment vector of the beam (i.e.$(\boldsymbol{q_i} - (\boldsymbol{q_i}.\boldsymbol{u}_{PQ})\boldsymbol{u}_{PQ})V_i$) which gives $-\left(\boldsymbol{u_{PQ}} \times (\boldsymbol{q_i} - (\boldsymbol{q_i}.\boldsymbol{u}_{PQ})\boldsymbol{u}_{PQ})\right)V_i$. The values of S_i, T_i and V_i for Timoshenko and Euler-Bernoulli beam theories are listed in Table 1. It is worth noting for a lateral rotational DOF, the procedure of obtaining the forces and moments is very similar to the aforementioned process and it could be easily done by replacing the terms S_i, T_i and V_i with the terms W_i, V_i and U_i, respectively.

In the following, the detailed procedure of derivation of the stiffness matrix elements for three distinct DOFs (q_1, q_2 and q_{10}) are presented. The derivation procedure of other DOFs is similar to the ones presented in the paper but are also provided in Section A.2 of the Appendix A.

a) First DOF: $\boldsymbol{q_1} = \mathbf{1}$

Here, the elements of the first column of the stiffness matrix by applying the unit displacement $q_1 = 1$ and by keeping all the other DOFs fixed (i.e. =0) are derived. This deformation type displaces point F_1 horizontally in the Z direction. This deformation only causes elongation in strut EF and it does not affect other struts. The vector of elongation of strut EF can be obtained by projecting the $\boldsymbol{q_1}$ vector on strut EF, i.e. $\left(\overrightarrow{q_1}.\frac{\overrightarrow{E_1F_1}}{|\overrightarrow{E_1F_1}|}\right)\frac{\overrightarrow{E_1F_1}}{|\overrightarrow{E_1F_1}|}$ or in a simpler notation: $(\boldsymbol{q_1}.\boldsymbol{u}_{E_1F_1})\boldsymbol{u}_{E_1F_1}$, where $\boldsymbol{q_1}$ is the unit vector parallel to the first

DOF and $\boldsymbol{u}_{E_1F_1}$ is the unit vector parallel to strut E_1F_1. The same system of notation will be used for the rest of the document. By multiplying the elongation vector of strut EF by the resultant force value of EF (S_1), the resultant force vector can be obtained as $\left((\boldsymbol{q_1}.\boldsymbol{u}_{E_1F_1})\boldsymbol{u}_{E_1F_1}\right)S_1$.

The equilibrium of forces at point F_1 in the q_1 direction, i.e. the Z direction, gives the K_{11} element of the stiffness matrix (Figure 6):

$$\sum F_{z,F_1} = 0 \rightarrow \frac{Q_1}{4} - \boldsymbol{q_1}.\left((\boldsymbol{q_1}.\boldsymbol{u}_{E_1F_1})\boldsymbol{u}_{E_1F_1}\right)S_1 = 0 \rightarrow K_{11} = Q_1 = 4S_1 \tag{2}$$

It must be noted that the forces demonstrated in Figure 6 are the forces which must act on the beam in order for it to deform as the way it is shown. The force the beam applied at each vertex is in the opposite direction of what is shown in figure. The same holds true for all the next derivations. The equilibrium of forces at point E_1 in the q_2 direction (i.e. in the Z direction) gives the K_{12} element of the stiffness matrix:

$$\sum F_{z,E_1} = 0 \rightarrow \frac{Q_2}{4} + \boldsymbol{q_2}.\left((\boldsymbol{q_1}.\boldsymbol{u}_{E_1F_1})\boldsymbol{u}_{E_1F_1}\right)S_1 = 0 \rightarrow K_{12} = Q_2 = -4S_1 \tag{3}$$

Since displacement of DOF q_1 does not have any effect on other DOFs ($q_3, q_4, q_5, q_6, q_7, q_8, q_9, q_{10}, q_{11}$), the remaining elements of first column of the stiffness matrix are zero.

b) Second DOF: $\boldsymbol{q_2 = 1}$

In this subsection, the elements of the second column of the stiffness matrix are derived. Therefore, we set $q_2 = 1$, and the other DOFs are set to zero. This deformation type displaces point E horizontally in the Z direction which causes strut EF to have pure contraction and strut ED to have contraction with transverse deformation. The vector of contraction of strut EF can be obtained by projecting vector $\boldsymbol{q_2}$ on strut EF, i.e. $(\boldsymbol{q_2}.\boldsymbol{u}_{E_1F_1})\boldsymbol{u}_{E_1F_1}$. The vector of contraction of strut ED can be obtained by projecting vector $\boldsymbol{q_2}$ on strut ED, i.e. $(\boldsymbol{q_2}.\boldsymbol{u}_{E_1D_1})\boldsymbol{u}_{E_1D_1}$, and the vector of transverse displacement of vertex E of strut ED can be calculated as $(\boldsymbol{q_2} - (\boldsymbol{q_2}.\boldsymbol{u}_{E_1D_1})\boldsymbol{u}_{E_1D_1})$.

By multiplying the contraction vector of strut EF by the resultant force value of EF (i.e. S_1), the resultant force vector for strut EF can be obtained as $\left((\boldsymbol{q_2}.\boldsymbol{u}_{E_1F_1})\boldsymbol{u}_{E_1F_1}\right)S_1$. Moreover, by multiplying the elongation vector of strut ED by the resultant force value of ED (S_2) the resultant force vector can be obtained as $\left((\boldsymbol{q_2}.\boldsymbol{u}_{E_1D_1})\boldsymbol{u}_{E_1D_1}\right)S_2$. As the final term, by multiplying the transverse deformation vector of strut ED by the resultant transverse force value of ED (T_2), the resultant transverse force vector for this strut can be obtained as $(\boldsymbol{q_2} - (\boldsymbol{q_2}.\boldsymbol{u}_{E_1D_1})\boldsymbol{u}_{E_1D_1})T_2$. It is worth noting that the resultant forces from deformation of struts ED at point E must be multiplied by four, as there are four similar struts ED connected to point E. The equilibrium of forces at point E in the q_2 direction (i.e. Z direction), Figure 7b, gives the K_{22} element of stiffness matrix:

$$\sum F_{z,E_1} = 0 \rightarrow \frac{Q_2}{4} - \boldsymbol{q_2}.\left((\boldsymbol{q_2}.\boldsymbol{u}_{E_1F_1})\boldsymbol{u}_{E_1F_1}\right)S_1 + 4\left(\boldsymbol{q_2}.\left((\boldsymbol{q_2}.\boldsymbol{u}_{E_1D_1})\boldsymbol{u}_{E_1D_1}\right)S_2\right) - 4(\boldsymbol{q_2}.(\boldsymbol{q_2} - (\boldsymbol{q_2}.\boldsymbol{u}_{E_1D_1})\boldsymbol{u}_{E_1D_1})T_2) = 0 \tag{4}$$

$$\rightarrow K_{22} = Q_2 = 4(S_1 + 4\sin^2\theta\, S_2 + 4\cos^2\theta\, T_2)$$

The reaction forces and moments at point D due to $\boldsymbol{q_2}$ leads to non-zero values of K_{25}, K_{26}, and K_{210}. By projecting the resultant contraction force vector $\left((\boldsymbol{q_2}.\boldsymbol{u}_{E_1D_1})\boldsymbol{u}_{E_1D_1}\right)S_2$ and the transverse deformation force vector $(\boldsymbol{q_2} - (\boldsymbol{q_2}.\boldsymbol{u}_{E_1D_1})\boldsymbol{u}_{E_1D_1})T_2$ of strut ED in q_5 and q_6 directions, and solving the equilibrium of forces at point D in these two directions, the elements K_{25} and K_{26} of the stiffness matrix could be obtained. It is important to note that the force vectors at point D have been multiplied by two (as two ED struts are connected to point D):

$$\sum F_{y,D_1} = 0 \ \rightarrow \ \frac{Q_5}{8} + 2\boldsymbol{q_5}.\left((\boldsymbol{q_2}.\boldsymbol{u}_{E_1D_1})\boldsymbol{u}_{E_1D_1}\right)S_2 + 2\boldsymbol{q_5}.(\boldsymbol{q_2} - (\boldsymbol{q_2}.\boldsymbol{u}_{E_1D_1})\boldsymbol{u}_{E_1D_1})T_2 = 0 \quad (5)$$

$$\rightarrow K_{25} = Q_5 = 4\sqrt{2}\sin 2\theta\,(T_2 - S_2)$$

$$\sum F_{q_6,D_1} = 0 \ \rightarrow \ \frac{Q_6}{8} + 2\boldsymbol{q_6}.\left((\boldsymbol{q_2}.\boldsymbol{u}_{E_1D_1})\boldsymbol{u}_{E_1D_1}\right)S_2 + 2\boldsymbol{q_6}.(\boldsymbol{q_2} - (\boldsymbol{q_2}.\boldsymbol{u}_{E_1D_1})\boldsymbol{u}_{E_1D_1})T_2 = 0 \quad (6)$$

$$\rightarrow K_{26} = Q_6 = 4\sin 2\theta\,(T_2 - S_2) - 8\sqrt{2}\sin^2\theta\, S_2 - 8\sqrt{2}\cos^2\theta\, T_2$$

To obtain the element K_{210} of the stiffness matrix, the equilibrium of moments in q_{10} direction at point D must be considered. The reaction moment vector, created by transverse deformation of point E of strut ED can be found by cross-product of unit vector of ED $\boldsymbol{u}_{E_1D_1}$ by the resultant moment vector of the beam at point D, i.e. $(\boldsymbol{q_2} - (\boldsymbol{q_2}.\boldsymbol{u}_{E_1D_1})\boldsymbol{u}_{E_1D_1})V_2$. This vector must be multiplied by two in the equilibrium equation as two struts ED are connected to point D. Finally, by solving the equilibrium of moments in the q_{10} direction, the element K_{210} of the stiffness matrix could be derived:

$$\sum M_{q_{10},D_1} = 0 \ \rightarrow \ \frac{Q_{10}}{8} + 2\boldsymbol{q_{10}}.\left(\boldsymbol{u}_{E_1D_1} \times (\boldsymbol{q_2} - (\boldsymbol{q_2}.\boldsymbol{u}_{E_1D_1})\boldsymbol{u}_{E_1D_1})\right)V_2 = 0 \quad (7)$$

$$\rightarrow K_{210} = Q_{10} = -8\cos\theta\, V_2$$

c) Tenth DOF: $\boldsymbol{q_{10}} = \mathbf{1}$

This DOF is another complex deformation in the structure as it applies rotation at vertex D which is connected to six struts (2×DC, 2×DE, DG, and DB). By projecting vector $\boldsymbol{q_{10}}$ on the noted struts, the torsion applied to each of the struts can be found $(\boldsymbol{q_{10}}.\boldsymbol{u}_{C_1D_1}, \boldsymbol{q_{10}}.\boldsymbol{u}_{E_1D_1}, \boldsymbol{q_{10}}.\boldsymbol{u}_{B_1D_1}, \boldsymbol{q_{10}}.\boldsymbol{u}_{G_1D_1})$. Then by multiplying the resultant torsion moments of each struts (W_2 and W_3), the torsion moment vectors could be obtained as $\left((\boldsymbol{q_{10}}.\boldsymbol{u}_{C_1D_1})\boldsymbol{u}_{C_1D_1}\right)W_3$, $\left((\boldsymbol{q_{10}}.\boldsymbol{u}_{E_1D_1})\boldsymbol{u}_{E_1D_1}\right)W_2$, $\left((\boldsymbol{q_{10}}.\boldsymbol{u}_{B_1D_1})\boldsymbol{u}_{B_1D_1}\right)W_2$, and

$\left((\boldsymbol{q}_{\mathbf{10}}.\boldsymbol{u}_{G_1D_1})\boldsymbol{u}_{G_1D_1}\right)W_3$. The extent of flexural rotation of struts DC, DE, DG and DB can be found by subtracting the torsion moment vector from vector $\boldsymbol{q}_{\mathbf{10}}$ which respectively gives $\boldsymbol{q}_{\mathbf{10}} - (\boldsymbol{q}_{\mathbf{10}}.\boldsymbol{u}_{C_1D_1})\boldsymbol{u}_{C_1D_1}$, $\boldsymbol{q}_{\mathbf{10}} - (\boldsymbol{q}_{\mathbf{10}}.\boldsymbol{u}_{E_1D_1})\boldsymbol{u}_{E_1D_1}$, $\boldsymbol{q}_{\mathbf{10}} - (\boldsymbol{q}_{\mathbf{10}}.\boldsymbol{u}_{B_1D_1})\boldsymbol{u}_{B_1D_1}$, and $\boldsymbol{q}_{\mathbf{10}} - (\boldsymbol{q}_{\mathbf{10}}.\boldsymbol{u}_{G_1D_1})\boldsymbol{u}_{G_1D_1}$. Afterwards, by multiplying the resultant bending moments of each strut (U_2 and U_3) to the noted terms, the lateral force vectors could be calculated. It is worth noting that the terms related to struts CD and ED must be multiplied by two, as two of such struts are connected to point D. Finally, by projecting all the resultant axial and lateral forces in the $\boldsymbol{q}_{\mathbf{10}}$ direction and writing the equation of moment equilibrium in this direction, the element K_{1010} can be found:

$$\begin{aligned}
&\sum M_{q_{10},D_1} = 0 \\
&\qquad \to \frac{Q_{10}}{8} - 2\boldsymbol{q}_{\mathbf{10}}.\left((\boldsymbol{q}_{\mathbf{10}}.\boldsymbol{u}_{C_1D_1})\boldsymbol{u}_{C_1D_1}\right)W_3 \\
&\qquad - 2\boldsymbol{q}_{\mathbf{10}}.(\boldsymbol{q}_{\mathbf{10}} - (\boldsymbol{q}_{\mathbf{10}}.\boldsymbol{u}_{C_1D_1})\boldsymbol{u}_{C_1D_1})U_3 \\
&\qquad - 2\boldsymbol{q}_{\mathbf{10}}.\left((\boldsymbol{q}_{\mathbf{10}}.\boldsymbol{u}_{E_1D_1})\boldsymbol{u}_{E_1D_1}\right)W_2 \\
&\qquad - 2\boldsymbol{q}_{\mathbf{10}}.(\boldsymbol{q}_{\mathbf{10}} - (\boldsymbol{q}_{\mathbf{10}}.\boldsymbol{u}_{E_1D_1})\boldsymbol{u}_{E_1D_1})U_2 \\
&\qquad - \boldsymbol{q}_{\mathbf{10}}.\left((\boldsymbol{q}_{\mathbf{10}}.\boldsymbol{u}_{B_1D_1})\boldsymbol{u}_{B_1D_1}\right)W_2 \\
&\qquad - \boldsymbol{q}_{\mathbf{10}}.(\boldsymbol{q}_{\mathbf{10}} - (\boldsymbol{q}_{\mathbf{10}}.\boldsymbol{u}_{B_1D_1})\boldsymbol{u}_{B_1D_1})U_2 \\
&\qquad - \boldsymbol{q}_{\mathbf{10}}.\left((\boldsymbol{q}_{\mathbf{10}}.\boldsymbol{u}_{G_1D_1})\boldsymbol{u}_{G_1D_1}\right)W_3 \\
&\qquad - \boldsymbol{q}_{\mathbf{10}}.(\boldsymbol{q}_{\mathbf{10}} - (\boldsymbol{q}_{\mathbf{10}}.\boldsymbol{u}_{G_1D_1})\boldsymbol{u}_{G_1D_1})U_3 = 0
\end{aligned} \tag{8}$$

$$\begin{aligned}
\to K_{1010} = Q_{10} &= 2((3 + \cos 2\varphi - 2\sqrt{2}\sin 2\varphi)W_3 + 2W_2(2\sin^2\theta + \cos^2\theta \\
&- 2\sqrt{2}\sin 2\theta) + 2\sqrt{2}\sin 2\theta U_2 - 2\cos^2\theta U_2 + (2(5 + \cos 2\theta)U_2 \\
&+ (9 - \cos 2\varphi + 2\sqrt{2}\sin 2\varphi)U_3))
\end{aligned}$$

The element K_{1011} could be obtained by solving the equilibrium of moments at vertex C. By projecting the reaction torsion and bending moment vectors created by rotation of vertex D of strut CD in the $\boldsymbol{q_{10}}$ direction and solving the equations of moment equilibrium in the same direction, the element K_{1011} could be calculated:

$$\sum M_{q_{11},C_1} = 0$$

$$\begin{aligned} &\rightarrow \frac{Q_{11}}{8} - 2\boldsymbol{q_{11}}.\left(\left(\boldsymbol{q_{10}}.\boldsymbol{u}_{C_1D_1}\right)\boldsymbol{u}_{C_1D_1}\right)W_3 \\ &- 2\boldsymbol{q_{11}}.\left(\boldsymbol{q_{10}} - \left(\boldsymbol{q_{10}}.\boldsymbol{u}_{C_1D_1}\right)\boldsymbol{u}_{C_1D_1}\right)\frac{U_3}{2} = 0 \end{aligned} \tag{9}$$

$$\rightarrow K_{1011} = Q_{11} = -4(2\sqrt{2}\cos^2\varphi - \sin 2\varphi)W_3 + 2(\sin 2\varphi + 2\sqrt{2}\sin^2\varphi)U_3$$

2.1.3 Stiffness matrix derivation

Finally, using the stiffness matrix elements obtained in Section 2.1.2 and also by considering the loading condition ($Q_8 = 2F$), the stiffness matrix and system of equations can be constructed as

$$\left\{\begin{matrix} 0 \\ 0 \\ 0 \\ 0 \\ 0 \\ 0 \\ 0 \\ 2F \\ 0 \\ 0 \\ 0 \end{matrix}\right\} = [A_{11} \quad A_{12} \quad A_{13}] \left\{\begin{matrix} q_1 \\ q_2 \\ q_3 \\ q_4 \\ q_5 \\ q_6 \\ q_7 \\ q_8 \\ q_9 \\ q_{10} \\ q_{11} \end{matrix}\right\} \tag{10}$$

where $[A_{11}]$,$[A_{12}]$ and $[A_{13}]$ are the partial matrices included in the overall stiffness matrix $[K]$. $[A_{11}]$,$[A_{12}]$ and $[A_{13}]$ have been used for easier representation of the overall stiffness matrix and are as follows:

$$A_{11} = \begin{bmatrix} 4S_1 & -4S_1 & 0 & 0 \\ -4S_1 & 4(S_1 + 4\sin^2\theta\, S_2 + 4\cos^2\theta\, T_2) & 0 & 0 \\ 0 & 0 & 8\sin^2\theta\, S_3 + 4(3 + \cos 2\varphi)T_3 & 8\sin^2\varphi\,(S_3 - T_3) \\ 0 & 0 & 8\sin^2\varphi\,(S_3 - T_3) & 8\sin^2\varphi\, S_3 + 4(3 + \cos 2\varphi])T_3 \\ 0 & \frac{16\cos\varphi\sin\theta\, L_3(-S_2 + T_2)}{L_2} & 8\sin^2\varphi\, S_3 + 4(3 + \cos 2\varphi)T_3 & 8\sin^2\varphi\,(S_3 - T_3) \\ 0 & -\frac{8\sqrt{2}(\cos\varphi\sin\theta\, L_3(S_2 - T_2) + L_2(\sin^2\theta\, S_2 + \cos^2\theta\, T_2))}{L_2} & 4\sqrt{2}\sin\varphi\,(\sqrt{2}\cos\varphi + \sin\varphi)(S_3 - T_3) & 4\sqrt{2}(\sin\varphi\,(\sqrt{2}\cos\varphi + \sin\varphi)S_3 - (-2 + \sqrt{2}\cos\varphi\sin\varphi + \sin^2\varphi)T_3) \\ 0 & 0 & 0 & 0 \\ 0 & 0 & 0 & 0 \\ 0 & 0 & 0 & 0 \\ 0 & -\frac{8\sqrt{2}\cos\varphi\, L_3V_2}{L_2} & -8(\sqrt{2}\cos\varphi + \sin\varphi)V_3 & 8\sin\varphi\, V_3 \\ 0 & 0 & -8\sqrt{2}\sin\varphi\, V_3 & 8\sqrt{2}\sin\varphi\, V_3 \end{bmatrix}$$

$$A_{12} = \begin{bmatrix} 0 & 0 & 0 & 0 \\ \frac{16\cos\varphi\sin\theta\, L_3(-S_2 + T_2)}{L_2} & -\frac{8\sqrt{2}(\cos\varphi\sin\theta\, L_3(S_2 - T_2) + L_2(\sin^2\theta\, S_2 + \cos^2\theta\, T_2))}{L_2} & 0 & 0 \\ 8\sin^2\varphi\, S_3 + 4(3 + \cos 2\varphi)T_3 & 4\sin\varphi\,(2\cos\varphi + \sqrt{2}\sin\varphi)(S_3 - T_3) & 0 & 0 \\ 8\sin^2\varphi\,(S_3 - T_3) & 4\sin\varphi\,(2\cos\varphi + \sqrt{2}\sin\varphi)S_3 - 4(-2\sqrt{2} + \sqrt{2}\sin^2\varphi + \sin 2\varphi)T_3 & 0 & 0 \\ 4(2\sin^2\theta\, S_2 + 2S_3 + \frac{4\cos^2\varphi\, L_3^2(S_2 - T_2)}{L_2^2} + 5T_2 + \cos 2\theta\, T_2 + 4T_3) & \frac{16\sqrt{2}\cos\varphi\sin\theta\, L_3(S_2 - T_2)}{L_2} + \frac{8\sqrt{2}\cos^2\varphi\, L_3^2(S_2 - T_2)}{L_2^2} + 4\sin\varphi\,(4\cos\varphi + \sqrt{2}\sin\varphi)(S_3 - T_3) & 8(\sin^2\theta\, S_2 + \cos^2\theta\, T_2) & 0 \\ \frac{16\sqrt{2}\cos\varphi\sin\theta\, L_3(S_2 - T_2)}{L_2} + \frac{8\sqrt{2}\cos^2\varphi\, L_3^2(S_2 - T_2)}{L_2^2} + 4\sin\varphi\,(4\cos\varphi + \sqrt{2}\sin\varphi)(S_3 - T_3) & 2(4\sin^2\theta\, S_2 + (5 - \cos 2\varphi + 2\sqrt{2}\sin 2\varphi)S_3 + \frac{8\cos\varphi\sin\theta\, L_3(S_2 - T_2)}{L_2} + \frac{12\cos^2\varphi\, L_3^2(S_2 - T_2)}{L_2^2} + 10T_2 + 2\cos 2\theta\, T_2 + 7T_3 + \cos 2\varphi\, T_3 - 2\sqrt{2}\sin 2\varphi\, T_3) & \frac{8\sqrt{2}\cos\varphi\sin\theta\, L_3(S_2 - T_2)}{L_2} & 0 \\ 8(\sin^2\theta\, S_2 + \cos^2\theta\, T_2) & \frac{8\sqrt{2}\cos\varphi\sin\theta\, L_3(S_2 - T_2)}{L_2} & 2(S_1 + 4\sin^2\theta\, S_2 + 4\cos^2\theta\, T_2) & -2S_1 \\ 0 & 0 & -2S_1 & 2S_1 \\ 8\cos\varphi\sin\varphi\,(-S_3 + T_3) & -8(\sin^2\varphi\, S_3 + \cos^2\varphi\, T_3) & 0 & 0 \\ -\frac{8\sqrt{2}(\sin\theta\, L_2 + 2\cos\varphi\, L_3)V_2}{L_2} - 8(\sqrt{2}\cos\varphi + 2\sin\varphi)V_3 & 8((\sin\theta + \frac{2\cos\varphi\, L_3}{L_2})V_2 + (\cos\varphi + \sqrt{2}\sin\varphi)V_3) & -\frac{8\sqrt{2}\cos\varphi\, L_3V_2}{L_2} & 0 \\ -8\sqrt{2}\sin\varphi\, V_3 & 8\sin\varphi\, V_3 & 0 & 0 \end{bmatrix}$$

And:

$$A_{13} = \begin{bmatrix} 0 & 0 & 0 \\ 0 & -\frac{8\sqrt{2}\cos\varphi\, L_3V_2}{L_2} & 0 \\ 0 & -8(\sqrt{2}\cos\varphi + \sin\varphi)V_3 & -8\sqrt{2}\sin\varphi\, V_3 \\ 0 & 8\sin\varphi\, V_3 & 8\sqrt{2}\sin\varphi\, V_3 \\ 8\cos\varphi\sin\varphi\,(-S_3 + T_3) & -\frac{8\sqrt{2}(\sin\theta\, L_2 + 2\cos\varphi\, L_3)V_2}{L_2} - 8(\sqrt{2}\cos\varphi + 2\sin\varphi)V_3 & -8\sqrt{2}\sin\varphi\, V_3 \\ -8(\sin^2\varphi\, S_3 + \cos^2\varphi\, T_3) & 8((\sin\theta + \frac{2\cos\varphi\, L_3}{L_2})V_2 + (\cos\varphi + \sqrt{2}\sin\varphi)V_3) & 8\sin\varphi\, V_3 \\ 0 & -\frac{8\sqrt{2}\cos\varphi\, L_3V_2}{L_2} & 0 \\ 0 & 0 & 0 \\ 8(\sin^2\varphi\, S_3 + \cos^2\varphi\, T_3) & -8\cos\varphi\, V_3 & 0 \\ -8\cos\varphi\, V_3 & \frac{2((3 + \cos 2\varphi - 2\sqrt{2}\sin 2\varphi)W_3L_2^2 + 4W_2(\sin\theta\, L_2 - \cos\varphi\, L_3)^2 + 8\cos\varphi\sin\theta\, L_2L_3U_2 - 4\cos^2\varphi\, L_3^2U_2 + L_2^2(2(5 + \cos 2\theta)U_2 + (9 - \cos 2\varphi + 2\sqrt{2}\sin 2\varphi)U_3))}{L_2^2} & -8\cos\varphi\,(\sqrt{2}\cos\varphi - \sin\varphi)W_3 + 4\sin\varphi\,(\cos\varphi + \sqrt{2}\sin\varphi)U_3 \\ 0 & -8\cos\varphi\,(\sqrt{2}\cos\varphi - \sin\varphi)W_3 + 4\sin\varphi\,(\cos\varphi + \sqrt{2}\sin\varphi)U_3 & 16(\cos^2\varphi\, W_3 + \sin^2\varphi\, U_3) \end{bmatrix} \tag{11}$$

2.1.4 Elastic properties relationships

All the unknown displacements and rotations q_1 to q_{11} can be obtained as functions of external force F_{UC} by inverting the final stiffness matrix $[K] = [\,[A_{11}] \quad [A_{12}] \quad [A_{13}]]$ and multiplying it by the force vector. Having the displacements as function of the applied force, elastic mechanical properties such as elastic modulus, Poisson's ratio, and yield stress of the unit cell can be obtained. The elastic modulus of unit cell can be calculated according to the basic definition of elastic modulus as follow:

$$E_{UC} = \frac{F_{UC} L_{UC}}{A_{UC} \delta_{UC}} \tag{12}$$

where $F_{UC}, L_{UC}, A_{UC}, \delta_{UC}$, and E_{UC} are the applied load, length, cross-sectional area, displacement, and elastic modulus of the re-entrant unit cell, respectively. By considering the $F_{UC} = F$, $\delta_{UC} = 2q_8$, $L_{UC} = 2(l_1 + l_3 \cos\varphi - l_2 \sin\theta)$ and $A_{UC} = {L_{UC}}^2$, the elastic modulus of re-entrant unit cell can be obtained as follow:

$$E_{UC} = \frac{F}{4(l_1 + l_3 \cos\varphi - l_2 \sin\theta) q_8} \tag{13}$$

Calculating q_8 from solving Equation (10) and inserting it in Equation (13) gives the elastic modulus relationship of the re-entrant unit cell. Since the final relationships for mechanical properties of the unit cell are very lengthy, the elastic modulus relationship for a specific case ($\theta = \varphi = 0°$, $r_1 = r_2 = r_3 = 0.14b$, and $l_1 = b$) is presented below:

$$E_{UC} = \frac{3\pi(9r^6(2(1+\sqrt{2})G_s + (13+9\sqrt{2})E_s) + 2b^2r^4(2(5+3\sqrt{2})G_s + (79+53\sqrt{2})E_s))}{2b^2(9r^4((26+24\sqrt{2})G_s + 7(23+16\sqrt{2})E_s) + 6b^2r^2((58+34\sqrt{2})G_s + (407+279\sqrt{2})E_s) + b^4(8(6+5\sqrt{2})G_s + (568+436\sqrt{2})E_s))} \tag{14}$$

Poisson's ratio of the unit cell, ν_{UC}, can be found by $-{}^{q_1}/_{q_8}$. So by calculating q_1 and q_8 from the inverse of Equation (10) and substituting them in this relationship, the Poisson's ratio formula for the unit cell can be found and the relationship for Poisson's ratio of the above-mentioned specific case ($\theta = \varphi = 0°$, $r_1 = r_2 = r_3 = 0.14b$ and also $l_1 = b$) can be obtained as follows:

$$\vartheta_{UC} = \frac{12(6+5\sqrt{2})b^4E_s + 6b^2r^2(2G_s + (5+\sqrt{2})E_s) - 9r^4(2G_s + (5+4\sqrt{2})E_s)}{9r^4((26+24\sqrt{2})G_s + 7(23+16\sqrt{2})E_s) + 6b^2r^2((58+34\sqrt{2})G_s + (407+279\sqrt{2})E_s) + b^4(8(6+5\sqrt{2})G_s + (568+436\sqrt{2})E_s)} \tag{15}$$

Evaluating the von Mises stress contours of FE models with several relative densities showed that vertices B of struts BD are the most critical points (the points with the maximum stress) in the structure. The yielding of the unit cell as a whole occurs when a point in the unit structure reached the yield stress of the bulk materials σ_{ys}. Therefore, the yield stress of the re-entrant unit cell can be obtained by assuming that the structure yielding occurs when the stress at point B of struts BD reaches the yield stress of the bulk material. Since struts BD are influenced by both bending moment and axial force (M_{DB}, F_{DB}), the maximum stress (σ_{max}) in end B of this strut could be calculated as follows:

$$\sigma_{max} = \frac{M_{DB}.r_2}{I_2} + \frac{F_{DB}}{A_2} \tag{16}$$

where r_2, I_2 and A_2 are the maximum distance of the strut cross-section from the neutral axis, area moment of inertia, and cross-sectional area of strut DB, respectively. To obtain the bending moment and axial force in strut DB, all of the lateral deformation and axial elongation of this strut applied by DOFs should be considered. DOFs q_5, q_6, and q_7 apply axial elongation and lateral displacement to ends B and D of this strut. Moreover, DOF q_{10} applies twist to point D. Eventually, the axial forces at point B of strut BD can be obtained as follow:

$$F_{DB} = (q_5 \sin\theta + q_6\, cos\, \theta + q_7 \sin\theta)S_2 \tag{17}$$

Similarly, the bending moments at point B of strut DB can be obtained as follows:

$$M_{DB} = (-q_5\, cos\, \theta + q_7\, cos\, \theta + q_6\, sin\, \theta)V_2 + (q_{10})U_2 \tag{18}$$

By substituting F_{DB} and M_{DB} from Equations (17) and (18) into equation (16) and inserting q_5, q_6, q_7, and q_{10} from solution of the inverse of Equation (10), the maximum local yield stress in strut DB can be obtained, and this relationship can be simplified for the specific case introduced above ($\theta = \varphi = 0°$, $r_1 = r_2 = r_3 = 0.14b$, and $l_1 = b$) as follows:

$$\sigma_{max} = \frac{F(2b^3r(2G_s - (1 + 2\sqrt{2})E_s) + 6b^2r^2(2(12 + 7\sqrt{2})G_s + 31(4 + 3\sqrt{2})E_s) - 3br^3(2G_s + (5 + 4\sqrt{2})E_s) + 18r^4(2G_s + (5 + 4\sqrt{2})E_s) + b^4(8(6 + 5\sqrt{2})G_s + (664 + 516\sqrt{2})E_s))}{36b\pi r^5(2(1 + \sqrt{2})G_s + (13 + 9\sqrt{2})E_s) + 8b^3\pi r^3(2(5 + 3\sqrt{2})G_s + (79 + 53\sqrt{2})E_s)} \tag{19}$$

Since the structure yield stress of re-entrant unit cell $\sigma_{y,UC}$ causes the maximum local yield stress σ_{max} at point B reach the bulk material yield stress $\sigma_{y,s}$, the normalized yield stress of the unit cell could be obtained by a cross-multiply of structure average stress $\sigma_{UC} = \frac{F_{UC}}{A_{UC}}$ and σ_{max} on one hand and the relevant yield stresses on the other hand:

$$\frac{\sigma_{y,UC}}{\sigma_{y,s}} = \frac{F_{UC}}{A_{UC}.\sigma_{max}} = \frac{F}{4(l_1 + l_3\cos\varphi - l_2\sin\theta)^2.\sigma_{Max}} \tag{20}$$

2.1.5 Effective lengths

One of the important considerations in deriving the analytical relationships of mechanical properties of structure is that the struts are connected rigidly to each other at the vertices of structures. Ideally, the struts are connected to each other from their very end points (vertices demonstrated in Figure 2a), and they do not interact with each other from any other point. However, practically, when several struts reach a vertex, as the cross-section area of the struts is non-zero, some volumes overlap with each other at the vertices which in turn decreases the effective lengths of struts which participate in the deformation of the structure. This phenomenon becomes of much more significance in auxetic materials, as there have very acute angles at the vertices (see for example Figure 2 and Figure 8)

In this study, the minimum distances between the joints were considered as the effective length of the struts. This definition for effective length was in accordance with what was observed in the stress and strain distribution of the structure obtained from the finite element (FE) results. In the following, the analytical derivation of effective lengths has been presented.

The effective length l_1 can be calculated by subtracting the size of intersection between Type-I and Type-II struts:

$$l_{1.eff} = l_1 - \frac{r_2}{cos\,\theta} - \frac{r_1}{tan\,\theta} \tag{21}$$

The effective length of Type-II strut is calculated by measuring the distance between the intersection of two Type-II struts at point D (struts DB and DE) and the intersection of Type-I and Type-II struts at point B (struts AB and BD), and it can be calculated by subtracting the intersecting lengths from l_2 as follows:

$$l_{2.eff} = l_2 - \frac{r_2}{tan\,{}^{\alpha_2}/_2} - r_1\,tan\,\theta \tag{22}$$

where α_2 is the angle between two Type-II struts.

Similarly, the effective length of Type-III strut occurs in intersection of Type-II and Type-III struts at point D (struts DC and DG) and the intersection of two Type-II struts at point C, and it can be calculated by subtracting the intersection lengths from l_3 as follow:

$$l_{3.eff} = l_3 - \frac{r_2}{sin\,\alpha_1} - \frac{r_3}{tan\,\alpha_1} \tag{23}$$

where α_1 is the angle between Type-II and Type-III struts.

By substituting these effective lengths into the stiffness matrix and resolving the system of equations (10), analytical relationships for mechanical properties of re-entrant unit cell can be obtained.

It is worth noting that the analytical relationships for angles α_1 and α_2 can be obtained as follow:

$$\alpha_1 = arccos\left(\frac{2l_3\cos^2\varphi + \sqrt{2}l_3\cos\varphi\sin\varphi + \sqrt{2}l_2\sin\varphi\sin\theta}{2l_2}\right) \tag{24}$$

$$\alpha_2 = arccos\left(\frac{l_3\cos\varphi\,(l_3\cos\varphi + 2l_2\sin\theta)}{{l_2}^2}\right) \tag{25}$$

2.2 Experimental tests

A Quantum Generous 3D printer with poly-lactic acid (PLA) filaments was used for manufacturing the test specimens. Since the mechanical properties of PLA could be different after printing process as compared to its properties in the original filament form, in order to obtain the mechanical properties of the bulk material, three types of cylindrical specimens were manufactured and tested under compression loading. The cylinders were printed in the horizontal (0°), vertical (90°) and inclined (45°) orientations with respect to the build plate direction. Four specimens were manufactured for each cylinder type (12 specimens in total). All the cylindrical specimens had the nominal length of 20 mm and diameter of 15 mm.

Three sets of re-entrant unit cell specimens with five different relative densities $\mu = 0.1$, 0.15, 0.2, 0.25, and 0.3 were manufactured (15 specimens in total). The dimensions of all the re-entrant unit cell specimens were 7.71 × 7.71 × 7.71 cm^3. All the specimens (unit cells and cylinders) were manufactured with a layer thickness of 100 μm and infill density of 100%. The static compression tests were performed using a SANTAM mechanical testing bench with a 20 kN load cell (Figure 8). The displacement rate was set to 0.1 mm/min. The normalized elastic modulus and normalized yield stress of specimens are obtained from load-displacement graphs, and the Poisson's ratio of unit cells are extracted from the side-view images.

Since the required forces for failure of the manufactured unit cells varied in the range of 750 N to 3700 N, to avoid the error causing by the deformation of the testing machine itself, all the tests were done with a large compression test machine (150 kN) for which the deformation in machine was negligible. More information on the effect of deformation of the mechanical test bench can be found in [40].

2.3 Numerical modelling

Two FE models were developed to calculate the mechanical properties of the re-entrant porous structures. Since analytical formulas of mechanical properties of unit cell have been derived based on Euler-Bernoulli and Timoshenko beam theories, the first FE model type was developed using Timoshenko beam elements (3D Quadratic finite strain beam, i.e. beam element type 189 in ANSYS) for discretizing the struts of unit cell. Timoshenko beam theory takes into account the transverse shear deformation. Each strut was divided into five beam elements. The struts were considered to be rigidly connected to each other at the vertices. The linear elastic material properties of the poly-lactic acid (PLA) obtained from the experimental test was adopted. The elastic modulus, Poisson's ratio, and yield stress of the beam elements were set to 1.93 GPa, 0.33, and 69 MPa, respectively. Periodic boundary conditions were implemented for the FE models of the re-entrant unit cells. For applying boundary conditions, the lowermost nodes of the unit cell at point A_2 (Figure 2a) were fully constrained in the all the transitional and rotational directions. The top node of the unit cell at point A_1 (Figure 2a) were displaced downwards, but they were not also allowed to have any horizontal displacement or rotation in any direction.

The second FE model type was developed using volumetric elements. This FE model would have a better representation of the overlapping effect at joints in the overall mechanical properties of structure. Five 3D models of re-entrant unit cell with geometries almost identical to the geometry of the manufactured samples (relative densities 0.1, 0.15, 0.2, 0.25, 0.3) were developed. An adaptive fine volumetric mesh was implemented for models to have a finer mesh at the vertexes and joint of the struts. To apply the loading and boundary condition, the lowermost face of the model (lower cross-sectional face of vertex A_2 of strut A_2B_2 in Figure 2) was fixed in all the directions and the top face of the model at point A_1 were displaced downwards. The material properties assigned to the volumetric elements was the same as those used in the first FE model.

In order to calculate the elastic modulus of the FE models, the sum of reaction force(s) at the lowermost node(s), F_{UC}, due to the vertical displacement of the top node(s), δ_{UC}, was measured and substituted in $E_{UC} = \frac{F_{UC}L_{UC}}{A_{UC}\delta_{UC}}$, where A_{UC} is the cross-sectional area of the FE model in the plane normal to the loading direction, and L_{UC} is the length of the FE structure in the direction parallel to the loading direction.

For obtaining the Poisson's ratio, the elongation of the structure in the lateral direction (X or Z direction) was divided by the contraction of the structure in the Y direction (loading direction).

Eventually, for obtaining the numerical normalized yield stress, the maximum stresses (von Mises stress) in strut DB of the unit cell was extracted (σ_{max}) and inserted into equation $\frac{F_{UC}}{A_{UC} \cdot \sigma_{max}}$.

3. Results

In this section, all the obtained analytical, numerical, and experimental results are presented and compared to each other. To have a better understanding of the main influencing factors on the over-all performance of the auxetic lattice structure, the effect of each main geometrical parameters of the structure such as relative density, angle θ, and angle φ are studied individually. Moreover, a lightened unit cell by eliminating the l_3 struts of the general 3D re-entrant unit cell is introduced and the mechanical properties of this unit cell are presented.

3.1 Effect of relative density

According to analytical relationships of mechanical properties of the re-entrant unit cell obtained in Section 2.1, elastic modulus, Poisson's ratio, and yield stress of the structure depend on seven geometrical main parameters, namely $r_1, r_2, r_3, l_1, l_2\ or\ l_3, \theta,$ and φ. To validate the analytical relationships, the mechanical properties of a specific case has been considered in which all the struts have the same radii ($r_1 = r_2 = r_3$), angles θ and φ are considered to be equal to $22.5°$, and $l_1 = b$ where b is shown in Figure 2b. It is worth noting that all the AM specimens have also been constructed according the above-mentioned geometrical parameters.

The analytical (based on Euler-Bernoulli and Timoshenko beam theories), numerical (based on beam and volumetric elements), and experimental results of this case have been presented and compared in Figure 9. The main factor shown in this figure is that both the Euler-Bernoulli and Timoshenko analytical models by considering effective length, the numerical model based on volumetric elements, and the experimental data points have good agreement with respect to each other. On the other hand, both the Euler-Bernoulli and Timoshenko analytical models without consideration of effective length and the numerical model based on beam elements (rather than volumetric elements) are close to each other but quite far from the experimental data points. As it can be seen in Figure 9, the analytical models considering the overlapping effect and the numerical models made from volumetric elements have higher levels of stiffness and yield stress, and lower levels of Poisson's ratio in comparison with the analytical models without considering overlapping effect and their equivalent numerical models which are based on beam elements.

As for the case of analytical relationships which neglect the overlapping effect at the vertices, it is evident that as compared to the analytical results based on Euler-Bernoulli beam theory, the analytical results based on Timoshenko beam theory have much better agreement with the beam-based FE model results for all of the relative densities (Figure 9). By increasing the relative density, the difference between numerical and analytical results for both beam theories increase, and the maximum difference between the numerical and analytical results (at relative density of $\mu = 0.4$) for normalized elastic modulus are 7.91% and 0.62% for Euler-Bernoulli and Timoshenko beam theories, respectively. As for the Poisson's ratio, the maximum difference between the beam-based FE model and the analytical models based on Euler-Bernoulli and Timoshenko beam theories are respectively 14.84% and 0.91%. It is worth noting that the maximum negative Poisson's ratio for this case is very high and equal to -0.7791. These numerical/analytical differences for normalized yield stress are 13.76% and 5.32% for Euler-Bernoulli and Timoshenko beam theories, respectively.

The maximum difference between the elastic modulus results of numerical models made from volumetric elements and the analytical models which consider the overlapping effect are 50.31% and 40.10% for Euler-Bernoulli and Timoshenko theories respectively (Figure 9b). Such differences for Poisson's ratio are 43.58% and 79.29% for Euler-Bernoulli and Timoshenko beam theories, respectively (Figure 9a). Finally, the noted differences for normalized yield stress are 37.95% and 17.82% for Euler-Bernoulli and Timoshenko beam theories, respectively (Figure 9c).

The mean value of the mechanical properties of the PLA filament obtained from compression tests on cylindrical specimens are presented in Table 2. All the auxetic specimens failed from the struts which were expected to have the maximum local stress in the unit cell (struts DB, Figure 10 shows the specimens from top view). The maximum differences between the experimental results and volumetric element numerical results for normalized elastic modulus, Poisson's ratio, and normalized yield stress are respectively

22.79%, 16.58%, and 15.59%, respectively. The maximum differences between the experimental results and Timoshenko analytical (by considering the overlapping effect) results for normalized elastic modulus, Poisson's ratio, and normalized yield stress are 21.09%, 26.14% and 4.06%, respectively.

Figure 11a shows the Von Mises stress distribution in the unit cell's struts for relative density of $\mu = 0.2$. According to this figure, it can be inferred that the maximum von Mises stress occurs in the same struts expected in analytical and numerical results with beam elements (struts BD). The stress distribution can be better visualized in the sliced unit cell in Figure 11b. The important point to note regarding the volumetric element numerical results is that the maximum stress locations are at the central point of vertex B (and experimental tests results). This, again, signifies the importance of considering the effective lengths rather than vertex-to-vertex length in the analytical models. The stress and strain distribution for all other unit cells with various relative densities have been presented in part B.4 and B.5 of appendix B.

3.2 Effect of angles θ and φ

Angles θ and φ are the most critical parameters in the 3D re-entrant structure as these parameters play the main role in creating the negative Poisson's ratio effect. Therefore, analyzing the effect of these parameters could be very beneficial for predicting the most extreme values of the mechanical properties, in particular, the negative Poisson's ratio. Figure 12, using 3D surface plot demonstration, presents variations in mechanical properties of 3D re-entrant unit cell with respect to angles θ and φ each varying in the range of -25 ° to +25 °. Moreover, the special cases of $\theta = 0°$, $\varphi = 0°$, and $\theta = \varphi$ are marked in the 3D plots with respectively solid, dash-dot, and dashed lines. All the plots are presented for $r_1 = r_2 = r_3 = 0.14b$ and with considering a constant volume for circumscribed cube of unit cell. Although one might assume that the mechanical properties of the unit should have symmetry with respect to angle θ, the results shown in Figure 12 demonstrate that the mechanical properties are not symmetrical with respect to $\theta = 0°$. Due to the constant volume assumed for circumscribed cube of unit cell, the length l_1 changes based on angle θ, and l_1 is shorter for $\theta < 0$ than for $\theta > 0$. Therefore, the results are not symmetrical with respect to $\theta = 0°$, and we have higher levels of normalized elastic modulus and yield stress for $\theta < 0$ as compared to $\theta > 0$. According to Figure 12a,c, the maximum normalized elastic modulus of 0.002234 occurs at $\theta = -25°$ and $\varphi = 2°$, and the maximum normalized yield stress of 0.008441 occurs at $\theta = -25°$ and $\varphi = 4.5°$. The behavior of Poisson's ratio with respect to variations of angles θ and φ is relatively different in comparison with elastic modulus and yield stress. As shown in Figure 12b, the maximum positive and negative values of Poisson's ratio occurs at $\theta = \varphi = -25°$ and $\theta = -\varphi = 25°$, respectively. The graph also shows that based on the proper combination of θ and φ, the structure can be either auxetic or non-auxetic and with the desired extent. Moreover, the graph shows that to have a near-zero Poisson's ratio, the angle θ needs to remain in the range of $4° < \theta < 8.5°$, while angle φ can take any value from $-25°$ to $+25°$. To better understand the effect of angles θ and φ on Poisson's ratio of re-entrant structure in other relative densities, the variations of Poisson's ratio for four relative densities ($r/b = 0.1$, $r/b = 0.2$, $r/b = 0.3$, and $r/b = 0.4$) are presented in Figure 13. According to this figure, the range of Poisson's ratio changes between -0.6 and $+0.2$ for $r/b = 0.1$. The range of change in Poisson's ratio gets much narrower for higher values of relative density. For instance, the minimum and maximum values of Poisson's ratio are -0.12 and +0.17 for $r/b = 0.4$. The influences of effective lengths on mechanical properties for various values of angles θ and φ could be found in part B.2 of Appendix B.

3.3 Effect of relative density on mechanical properties of the special case with $\boldsymbol{\theta = \varphi = 0°}$

A critical case can be considered for the re-entrant structure in which angles θ and φ are considered to be zero. The effect of variation in relative density of such structure has been plotted in Figure 14. The figure shows that in case of neglecting the over-lapping effect, the analytical results based on Timoshenko beam theory have better agreement in comparison with Euler Bernoulli beam theory with numerical results based on beam elements model for all values of relative density. According to Figure 14a, the re-entrant structure does not have negative Poisson's ratio, and the value of Poisson's ratio for all relative densities is positive and varies from 0.127 to 0.074. Considering the overlapping effect decreases the values of Poisson's ratio and the minimum value of Poisson's ratio for this case reaches 0.00894.

3.4 Elimination of struts l_3

According to the contours of mechanical properties of 3D re-entrant unit cell shown in Figure 13, the angle φ had negligible effect on the sign of Poisson's ratio in all values of $r/_b$, see. This gives an inspiration to create a new lightened re-entrant unit cell by eliminating struts l_3 from the general 3D re-entrant unit cell. The lightened unit cell with negative, zero, and positive values of θ are shown in Figure 15. The analytical relationships for this unit cell could be easily obtained by setting $r_3 = 0$ in the general relationships (i.e. Eqs. (14), (15) and (19)). The resulting mechanical properties of the lightened re-entrant unit cell are presented in Figure 16. The results show that the maximum normalized elastic modulus and yield stress for lightened unit cell occur in θ=+25 ° for all values of relative densities. The maximum negative and positive Poisson's ratio for lightened unit cell is obtained as -0.6322 and +0.352, respectively. The variations of mechanical properties of lightened unit cell with respect to relative density in special condition of $\theta = 0$ have been presented with solid lines in the Figure 16. Similar to the general unit cell, the lightened structure has positive Poisson's ratio for all values of relative densities in $\theta = 0$, and the value of Poisson's ratio for this case varies from 0.1688 to 0.09837 (Figure 16b).

Comparison of the general idealized 3D re-entrant unit cell and lightened 3D re-entrant unit cell can give a good insight for designers to decide which design to choose from. For quantitative comparison, the comparisons are performed for the unit cells with the mean values of relative density and r/b, i.e. $\mu = 0.25$ and $r/b = 0.25$. As for the case of $\mu = 0.25$, the value of normalized elastic modulus in $\theta = 25°$ were calculated as 0.006095 and 0.009178 for general re-entrant and lightened structures, respectively. As for the case of $r/b = 0.25$, the values of normalized elastic modulus were obtained as 0.005367 and 0.004184 for general re-entrant and lightened structures, respectively (Figure B4a, Appendix B). Moreover, the normalized yield strength at $\mu = 0.25$ were 0.007666 and 0.01157 for general re-entrant and lightened structures, respectively (Figure B6c, Appendix B), while at $r/b = 0.25$, they were 0.006837 and 0.005808, respectively (Figure B4c, Appendix B). Therefore, based on results, we can conclude that the lightened structure has better strength and stiffness at the same relative densities in comparison with general structure. In contrast, the lightened unit cell is weaker than the general re-entrant structure at same ratio of r/b. This comparison could be done for Poisson's ratio as well. At the same relative density of $\mu = 0.25$ and $\theta = 25°$, Poisson's ratio of the general structure and lightened structures were obtained as -0.2191 and -0.2673, respectively. These values at the conditions of $r/b = 0.25$ and $\theta = 25°$ were -0.2318 and -0.3419 for the general and lightened structures, respectively (Figure B4b, Appendix B). Therefore, eliminating struts l_3 always increases the extent of either the positive or negative values of Poisson's ratio for both the cases of identical relative densities and r/b ratio. Additional data and figures for comparison between the general re-entrant structure and lightened structure could be found in Section B.3 of Appendix B (Figures B4 - B7).

4. Discussions

4.1. Why the Timoshenko relationships have better accuracy?

In this paper, the relationships based on Timoshenko beam theory have been derived for elastic modulus, Poisson's ratio, and yield strength of re-entrant lattice structure. Based on the presented results in all cases of studies and also in the all relative densities of structure, the Timoshenko beam theory presents better and more precise results for mechanical properties of lattice structure in comparison with the Euler-Bernoulli beam theory. The main reason of accuracy of Timoshenko theory is that this theory takes into account shear deformation and rotational bending effects, making it suitable for describing the behavior of thick beams. For this reason, the analytical results of mechanical properties of system based on Euler-Bernoulli in higher values of relative densities deviates from numerical results and the Timoshenko beam theory overlap with numerical results in all values of relative densities. It worth be noted that taking into account the shear mechanisms of deformation effectively lowers the stiffness of the struts and structure which yields to larger deflections of the struts under a static load. This causes higher and lower Poisson's ratio and elastic modulus of the structure for Timoshenko theory in comparison with Euler-Bernoulli beam theory.

4.2. The most influencing parameters on structure Poisson's ratio.

In general, angles θ and φ are the main design parameters in creating negative Poisson's ratio effect in the re-entrant structure. According to the results (Figure 12 and Figure 13), the magnitude of θ determines the sign of Poisson's ratio (positive or negative). Moreover, increasing θ leads to more negative values of Poisson's ratio in the unit cell. It is important to note that even though the value of φ has some effects on the amount of Poisson's ratio, but it does not have any effects on the sign of the Poisson's ratio. It is worth noting that there is a specific case (specific values for θ and φ) in the re-entrant structure which in this case the Poisson's ratio of structure becomes zero.

Considering the effective length in the analytical calculations decreases the effects of θ and φ, which is more similar to what would be experienced in real-life conditions (as also confirmed by numerical models based on volumetric elements and experimental results). More importantly, the effect of variation in φ on Poisson's ratio is almost eliminated when the effective length is taken into consideration (see part B.2 of Appendix B).

According to stress distribution observation in the re-entrant structure, struts BD are the most influential elements in determining the sign and value of the transverse deformation of unit cell. Applied load at points A of unit cell is directly transferred to points B of struts BD via struts AB and this causes struts BD have normal tensile stress as shown in Figure 17. However, struts CD are under compressive normal stress due to the load applied to the structure. This makes struts CD demonstrate inverse behavior and to resist negative Poisson's ratio of the system. Therefore, the effect of θ on Poisson's ratio is much greater than that of φ in both conditions (either effective lengths are considered or not).

The other effective parameter in Poisson's ratio of structure is relative density: the higher the relative density, the lower the negative Poisson's ratio will be. An ideal model (analytical beam model without consideration of vertex overlapping) has negative Poisson's ratio in all values of relative densities, but in more realistic models, and particularly in higher relative densities, (very small) positive Poisson's ratios can be observed. This is due to the positive Poisson's ratio of the bulk material (PLA) which takes more dominance in the structural deformation of system in higher relative densities.

4.3. Differences between general 3D re-entrant structures and lightened 3D structure.

Based on the normal and bending stress distribution in the struts of structure shown in Figure 17, it was predictable that eliminating struts CD from the system could contribute to increase in the value of Poisson's ratio in unit cell, even though it will lead to decrease in the strength and stiffness of the structure. According to comparison results presented in Figures B4 and B5 of Appendix B, the stiffness and strength of the lightened structures resulted from eliminating struts CD are lower than the general re-entrant structure in the same values of r/b. However, it must be mentioned that the mechanical properties of the lattice structures and metamaterials are usually compared with each other at similar relative densities. Thus, Figures B6 and B7 could be a better reference for comparison of the stiffness and strength of the general re-entrant and lightened unit cells. According to these figures, we can conclude that at the same relative densities, the lightened structure could be a better option in comparison with the general structure due to its higher elastic modulus and yields stress. In addition, the results show that the lightened structure could provide higher values of negative or positive Poisson's ration either in the same relative density or r/b ratio.

All of the above-mentioned comparisons are based on the assumed condition of $\theta = \varphi$ in general 3D re-entrant structure. Therefore, it should be emphasized that the general re-entrant structure can present a much wider range of mechanical properties for $\theta \neq \varphi$ as compared to lightened unit cell due to its additional parameters φ and l_3. Moreover, with a proper choice of θ and φ values, the general structure can present ideal modulated mechanical properties with desired combination of mechanical properties (Poisson's ratio, elastic modulus, and yield strength). For instance, as it can be seen in Figure 12b, angle φ has a relatively low effect on Poisson's ratio (θ is the governing parameter here), while it has a huge effect on elastic modulus and yield strength. Therefore, as compared to lightened structure, the general re-entrant unit cell has the advantage of giving the opportunity of designing a structure with desirable combination of elastic modulus and Poisson's ratio.

4.4. Some points regarding effective length (Definition, effect, errors, etc.)

All the struts in analytical solution of the structures were considered as links, and they were considered to be rigidly connected to each other at the vertices. However, in practice, when the struts reach each other at the joints, they overlap each other and in fact the lengths which contribute to the deformation of struts and the structure as a whole is decreased. Generally, there is no accurate definition for the effective length, and in this study, the minimum distance between the start and end points of struts which are not in the overlapping regions have been considered as strut effective length. This definition has been chosen based on the stress and strain distribution in the struts of the volumetric numerical models. The effective lengths have been defined from the regions of the struts which stress and strain values start to increase abruptly. By considering the effective length, the analytical results give much better agreement with experimental test results which can be very helpful to analyzing the structure in real-life conditions.

5. Conclusions

In this paper, a new complex 3D re-entrant structure with negative Poisson's ratio was studied and analytical relationships for its elastic mechanical properties (elastic modulus, yield strength, and Poisson's ratio) were derived. Two different FE models one based on beam element and the other based on volumetric elements were implemented for analyzing and validating the analytical results. Five sets of specimens with different relative density values were also additively manufactured and tested under compressive loading condition, and the obtained experimental data were used for analysis of the behavior of structure in actual conditions. The analytical results based on effective length had good agreement with volumetric numerical model and experimental results. Finally, the effect of various parameters on the mechanical properties of the structure was studied and the results demonstrated that angle θ has the most effect on the sign of the Poisson's ratio, while angle φ has minimal effect on Poisson's ratio. However, the struts corresponding to angle φ provide strength and stiffness for the structure. The results also showed that the structure could have zero Poison's ratio for a specific range of θ and φ angles. In the end, a lightened re-entrant structure was introduced and its results were compared to those of the idealized 3D re-entrant structure.

REFERENCES

1. Roh, J., et al., *Failure of classical elasticity in auxetic foams.* AIP Advances, 2013. **3**(4): p. 042126.
2. Wojciechowski, K.W. and V.V. Novikov, *Negative Poisson's ratio and percolating structures.* Task Quarterly, 2001. **5**(1): p. 5-11.
3. Gercek, H., *Poisson's ratio values for rocks.* International Journal of Rock Mechanics Mining Sciences, 2007. **44**(1): p. 1-13.
4. Milton, G.W., *Composite materials with Poisson's ratios close to—1.* Journal of the Mechanics Physics of Solids, 1992. **40**(5): p. 1105-1137.
5. Caddock, B. and K. Evans, *Microporous materials with negative Poisson's ratios. I. Microstructure and mechanical properties.* Journal of Physics D: Applied Physics, 1989. **22**(12): p. 1877.
6. Kimizuka, H., H. Kaburaki, and Y. Kogure, *Mechanism for negative Poisson ratios over the α-β transition of cristobalite, SiO 2: a molecular-dynamics study.* Physical review letters, 2000. **84**(24): p. 5548.
7. Baughman, R.H., et al., *Negative Poisson's ratios as a common feature of cubic metals.* Nature

1998. **392**(6674): p. 362-365.
8. Grima, J.N., et al., *Do zeolites have negative Poisson's ratios?* Advanced Materials, 2000. **12**(24): p. 1912-1918.
9. Yeganeh-Haeri, A., D.J. Weidner, and J.B. Parise, *Elasticity of α-cristobalite: a silicon dioxide with a negative Poisson's ratio.* Science, 1992. **257**(5070): p. 650-652.
10. Alderson, A. and K.E. Evans, *Molecular origin of auxetic behavior in tetrahedral framework silicates.* Physical review letters, 2002. **89**(22): p. 225503.
11. Williams, J. and J. Lewis, *Properties and an anisotropic model of cancellous bone from the proximal tibial epiphysis.* Transactions of the ASME, 1982. **104**.
12. Gatt, R., et al., *Negative Poisson's ratios in tendons: an unexpected mechanical response.* Acta biomaterialia, 2015. **24**: p. 201-208.
13. Veronda, D. and R. Westmann, *Mechanical characterization of skin—finite deformations.* Journal of biomechanics, 1970. **3**(1): p. 111-124.
14. Lees, C., J.F. Vincent, and J.E. Hillerton, *Poisson's ratio in skin.* Bio-medical materials engineering, 1991. **1**(1): p. 19-23.
15. Hedayati, R., et al., *Action-at-a-distance metamaterials: Distributed local actuation through far-field global forces.* APL Materials, 2018. **6**(3): p. 036101.

16. Hedayati, R., et al., *Semianalytical geometry-property relationships for some generalized classes of pentamodelike additively manufactured mechanical metamaterials.* Physical Review Applied, 2019. **11**(3): p. 034057.
17. Li, J. and C. Chan, *Double-negative acoustic metamaterial.* Physical Review E, 2004. **70**(5): p. 055602.
18. Ding, Y., et al., *Metamaterial with simultaneously negative bulk modulus and mass density.* Physical review letters, 2007. **99**(9): p. 093904.
19. Kolken, H.M. and A. Zadpoor, *Auxetic mechanical metamaterials.* RSC advances, 2017. **7**(9): p. 5111-5129.
20. Hedayati, R., S.A. Yavari, and A. Zadpoor, *Fatigue crack propagation in additively manufactured porous biomaterials.* Materials Science and Engineering: C, 2017. **76**: p. 457-463.
21. Hedayati, R., et al., *Comparison of elastic properties of open-cell metallic biomaterials with different unit cell types.* Journal of Biomedical Materials Research Part B: Applied Biomaterials, 2017.
22. Zadpoor, A.A., *Mechanical meta-materials.* Materials Horizons, 2016. **3**(5): p. 371-381.
23. Lee, J.H., J.P. Singer, and E.L. Thomas, *Micro-/nanostructured mechanical metamaterials.* Advanced materials, 2012. **24**(36): p. 4782-4810.
24. Yang, L., et al., *Additive manufacturing of metal cellular structures: design and fabrication.* Jom, 2015. **67**(3): p. 608-615.
25. Smith, D.R., J.B. Pendry, and M.C. Wiltshire, *Metamaterials and negative refractive index.* Science, 2004. **305**(5685): p. 788-792.
26. Evans, K.E. and A. Alderson, *Auxetic materials: functional materials and structures from lateral thinking!* Advanced materials, 2000. **12**(9): p. 617-628.
27. Whitty, J., F. Nazare, and A. Alderson, *Modelling the effects of density variations on the in-plane Poisson's ratios and Young's moduli of periodic conventional and re-entrant honeycombs-Part 1: Rib thickness variations.* Cellular Polymers, 2002. **21**(2): p. 69-98.
28. Alderson, A., et al., *An auxetic filter: a tuneable filter displaying enhanced size selectivity or defouling properties.* Industrial engineering chemistry research, 2000. **39**(3): p. 654-665.
29. Wan, H., et al., *A study of negative Poisson's ratios in auxetic honeycombs based on a large deflection model.* European Journal of Mechanics-A/Solids

2004. **23**(1): p. 95-106.

30. Mirzaali, M., et al., *Rational design of soft mechanical metamaterials: Independent tailoring of elastic properties with randomness.* Applied Physics Letters, 2017. **111**(5): p. 051903.
31. Yang, L., et al., *Compressive properties of Ti–6Al–4V auxetic mesh structures made by electron beam melting.* Acta Materialia, 2012. **60**(8): p. 3370-3379.
32. Critchley, R., et al., *The Preparation of Auxetic Foams by Three-D imensional Printing and Their Characteristics.* Advanced Engineering Materials, 2013. **15**(10): p. 980-985.
33. Farokhi Nejad, A., et al., *Using Finite Element Approach for Crashworthiness Assessment of a Polymeric Auxetic Structure Subjected to the Axial Loading.* Polymers, 2020. **12**(6): p. 1312.
34. Yang, L., et al., *Mechanical properties of 3D re-entrant honeycomb auxetic structures realized via additive manufacturing.* International Journal of Solids Structures, 2015. **69**: p. 475-490.
35. Wang, X.-T., X.-W. Li, and L. Ma, *Interlocking assembled 3D auxetic cellular structures.* Materials Design, 2016. **99**: p. 467-476.
36. Chen, Y. and M.-H. Fu, *A novel three-dimensional auxetic lattice meta-material with enhanced stiffness.* Smart Materials Structures, 2017. **26**(10): p. 105029.
37. Xue, Y., et al., *An Enhanced Three-Dimensional Auxetic Lattice Structure with Improved Property.* Materials Design, 2020. **13**(4): p. 1008.
38. Lakes, R.J.S., *Foam structures with a negative Poisson's ratio.* 1987. **235**: p. 1038-1041.

39. Berwind, M.F., A. Kamas, and C. Eberl, *A hierarchical programmable mechanical metamaterial unit cell showing metastable shape memory.* Advanced Engineering Materials, 2018. **20**(11): p. 1800771.
40. Hedayati, R., et al., *Isolated and modulated effects of topology and material type on the mechanical properties of additively manufactured porous biomaterials.* Journal of the mechanical behavior of biomedical materials, 2018.
41. Hedayati, R., et al., *Improving the accuracy of analytical relationships for mechanical properties of lattice structures.* Submitted, 2019.

Tables

Table 1: Parameters defined for summarizing the relationships for Euler-Bernoulli and Timoshenko beam theories

Term	Euler-Bernoulli Theory	Timoshenko Theory
S_i	$\frac{A_i E_s}{l_i}$	$\frac{A_i E_s}{l_i}$
W_i	$\frac{G_s J_i}{l_i}$	$\frac{G_s J_i}{l_i}$
T_i	$\frac{12 E_s I_i}{l_i^3}$	$\frac{1}{\frac{l_i^3}{12 E_s I_i} + \frac{l_i}{\kappa A_i G_s}}$
V_i	$\frac{6 E_s I_i}{l_i^2}$	$\frac{1}{\frac{l_i^2}{6 E_s I_i} + \frac{2}{\kappa A_i G_s}}$
U_i	$\frac{4 E_s I_i}{l}$	$\frac{\frac{2 E_s I_i}{\kappa A_i G_s l} + \frac{2 l_i}{3}}{\frac{l_i^2}{6 E_s I_i} + \frac{2}{\kappa A_i G_s}}$

Table 2: Elastic properties of cylindrical specimens made of PLA filaments.

Property	0°	45°	90°
Elastic modulus (GPa)	2.016	1.964	1.824
Yield stress (MPa)	74.67	73.6	63.67

Figures

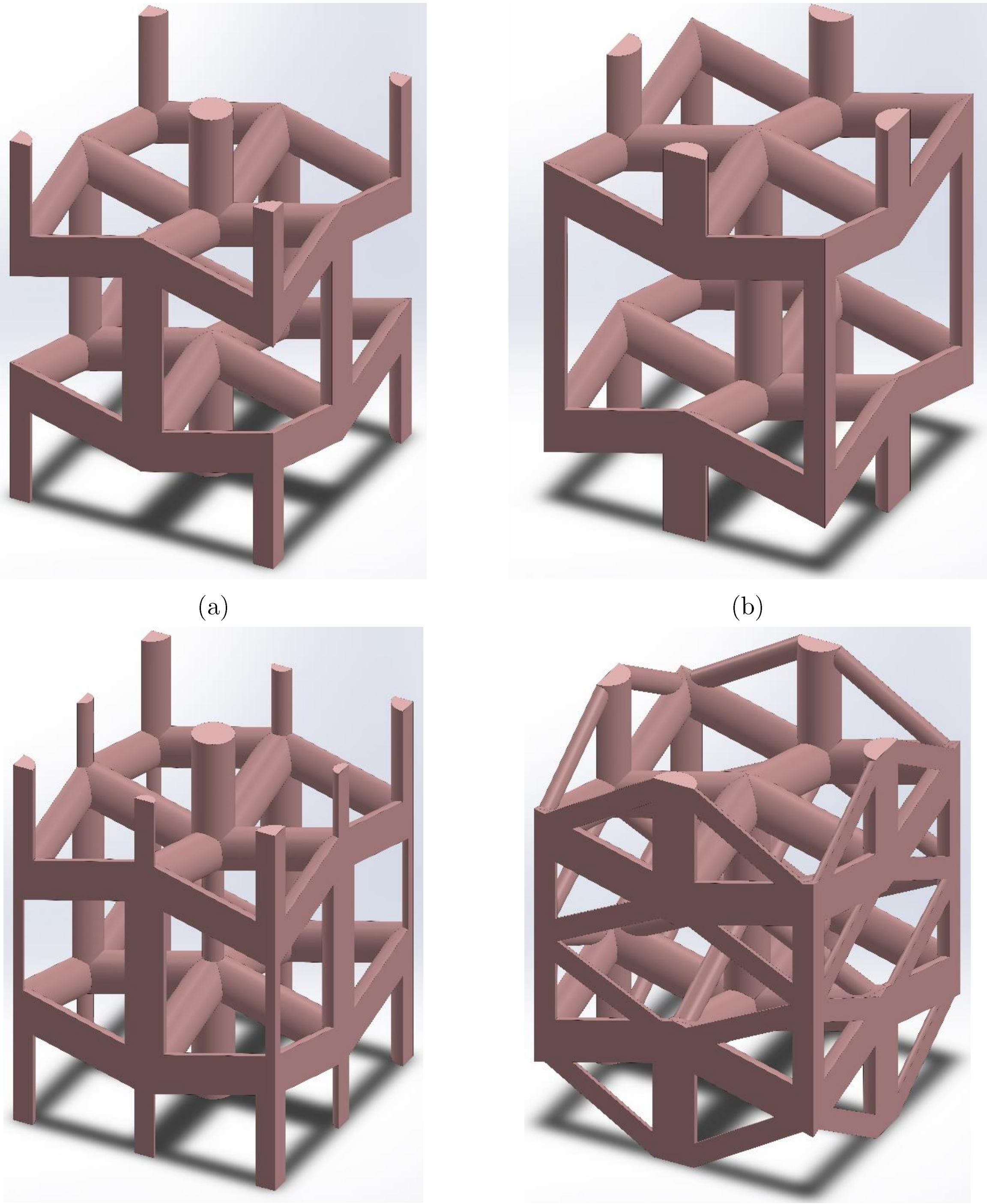

(a) (b)

(c) (d)

Figure 1: Review of 3D re-entrant unit cells: (a) Li Yang et al. (2015) [34], (b) Xin-Tao Wang et al. (2016) [35], (c) Yu Chen et al. (2017) [36], (d) Yingying Xue et al. (2020) [37]

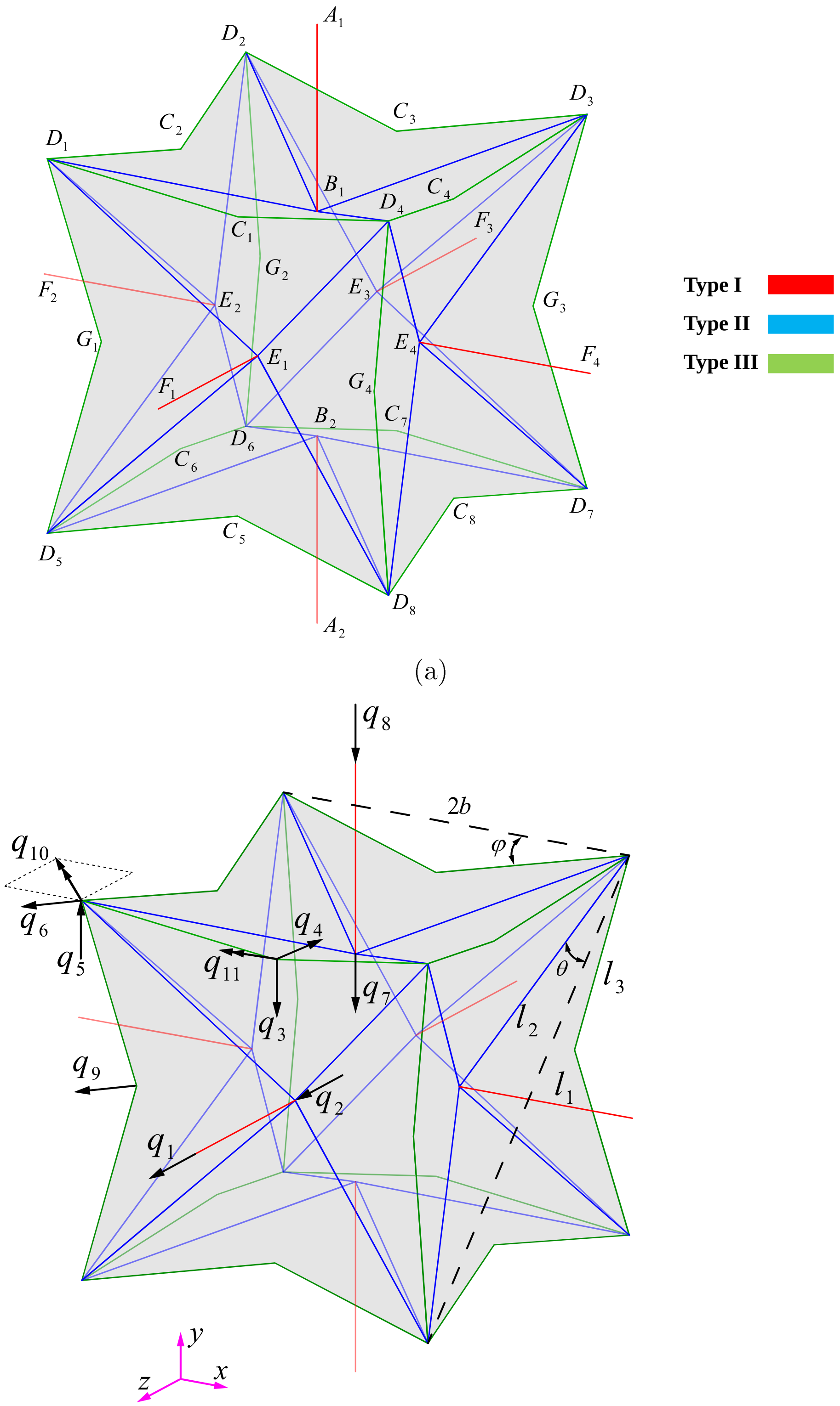

(a)

(b)

Figure 2: (a) An idealized 3D re-entrant unit cell and its strut types, (b) DOFs of the unit cell

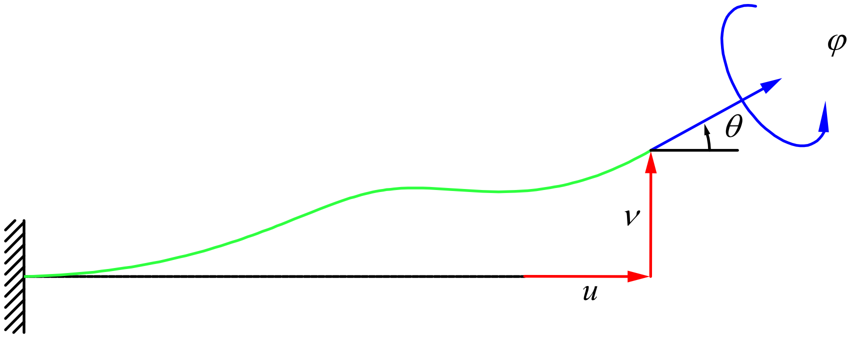

Figure 3- General deformation of a cantilever beam with axial and lateral displacements as well as flexural and torsional rotations in the free end

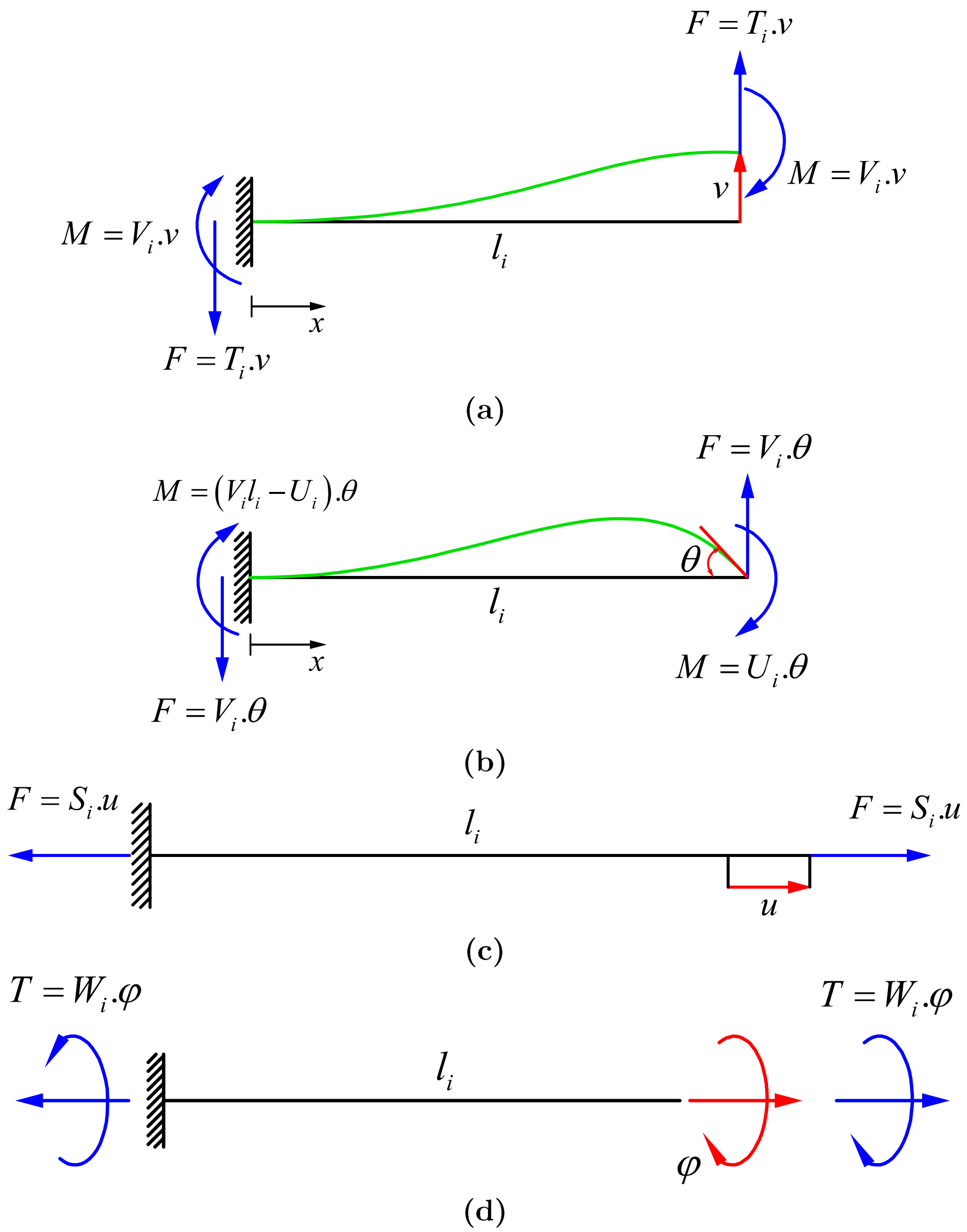

*Figure 4- Forces and moments required to cause (a) lateral displacement **δ** with no rotation, (b) rotation **θ** with no lateral displacement, (c) pure axial extension, and (d) pure twist at the free end of a beam [41]*

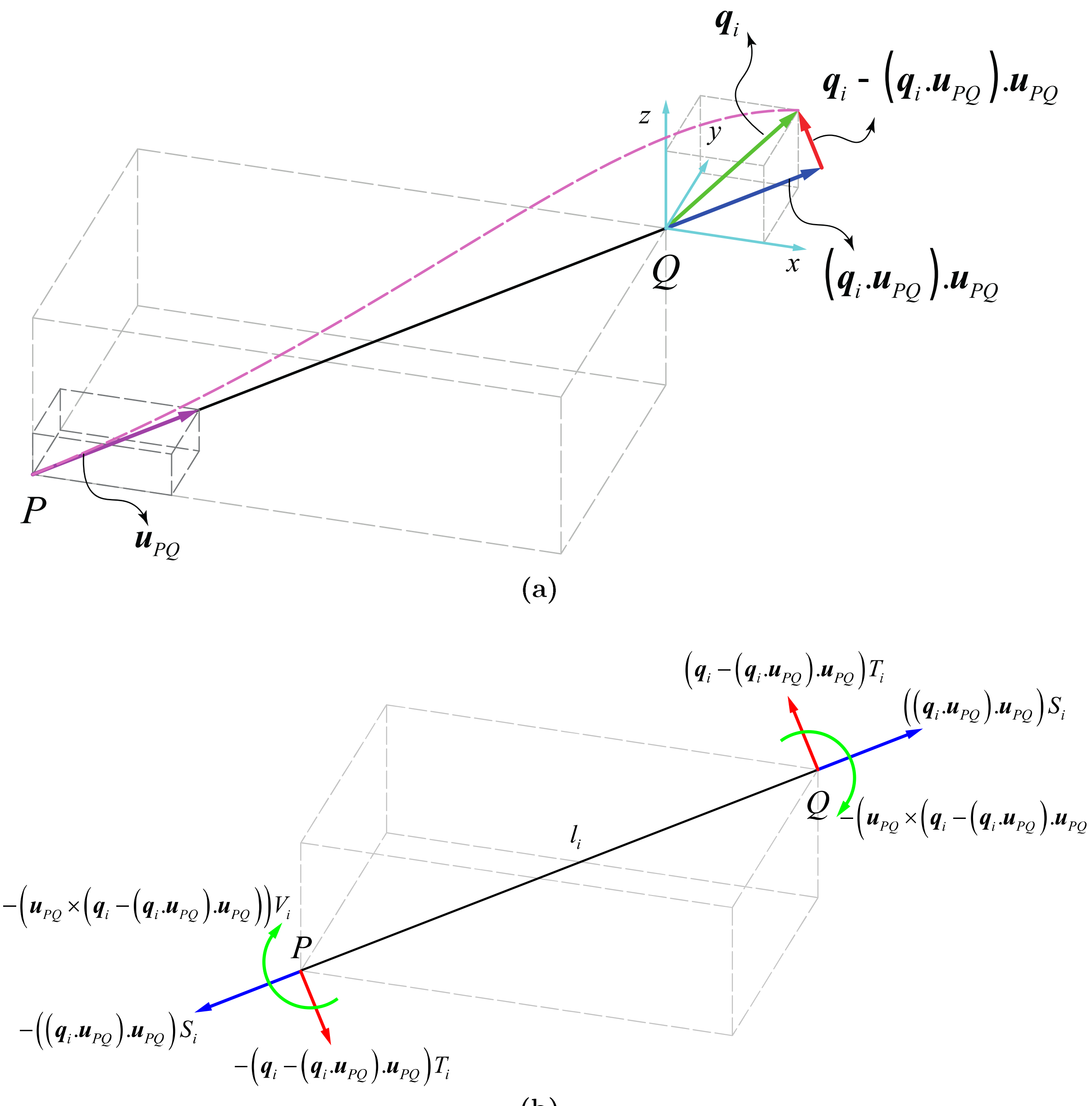

Figure 5- General deformation of a strut due to $\mathbf{q_i = 1}$ (a) magnitude of deformations (b) resultant forces and moments

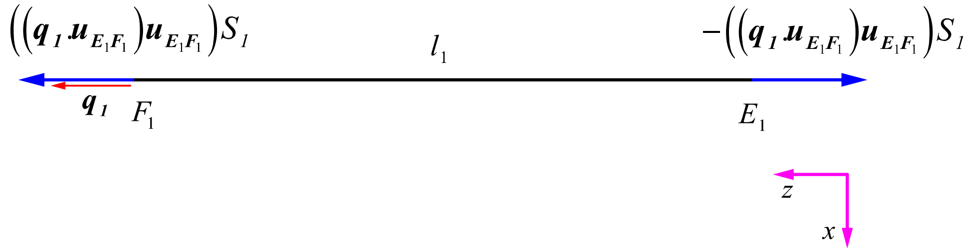

Figure 6- Deformation of strut EF due to $\mathbf{q_1 = 1}$.

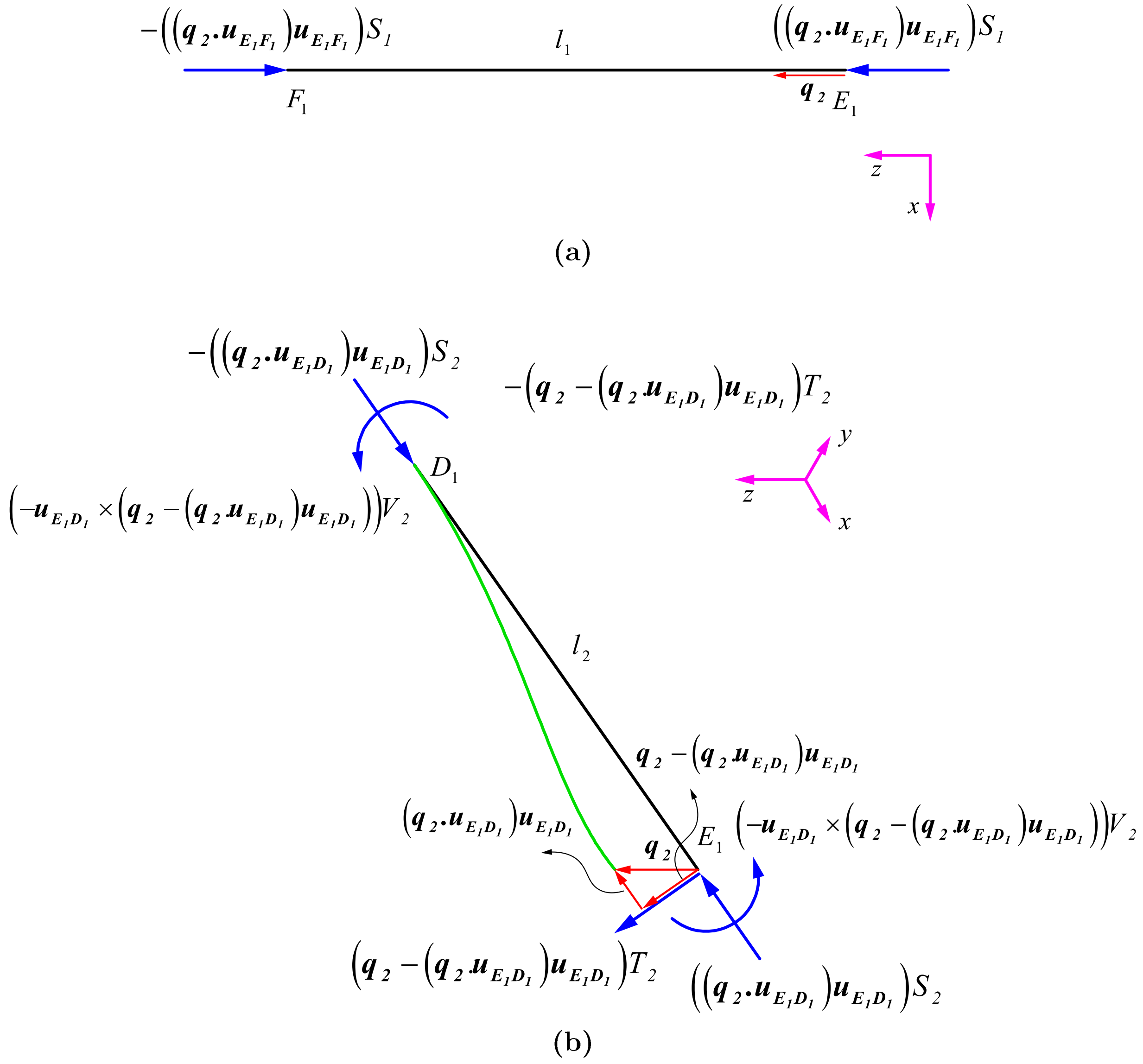

Figure 7- Deformation of (a) strut EF and (b) strut ED due to $\mathbf{q_2 = 1}$***.***

Figure 8: Test sample with $\boldsymbol{\mu} = \mathbf{0.25}$ under compression testing

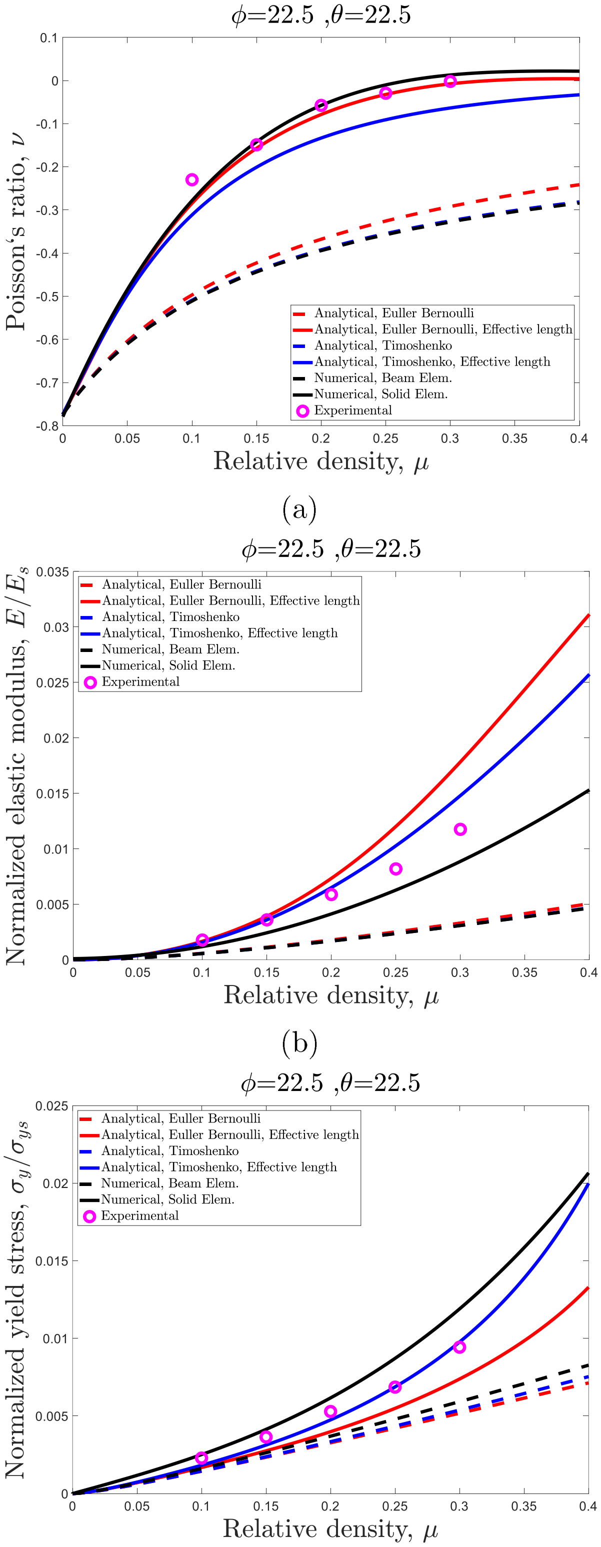

(a)

(b)

(c)

Figure 9: Mechanical properties curves of 3D re-entrant structure with $\boldsymbol{\varphi} = \mathbf{22.5}$, $\boldsymbol{\theta} = \mathbf{22.5}$: (a) elastic modulus, (b) Poisson's ratio, and (c) yield stress.

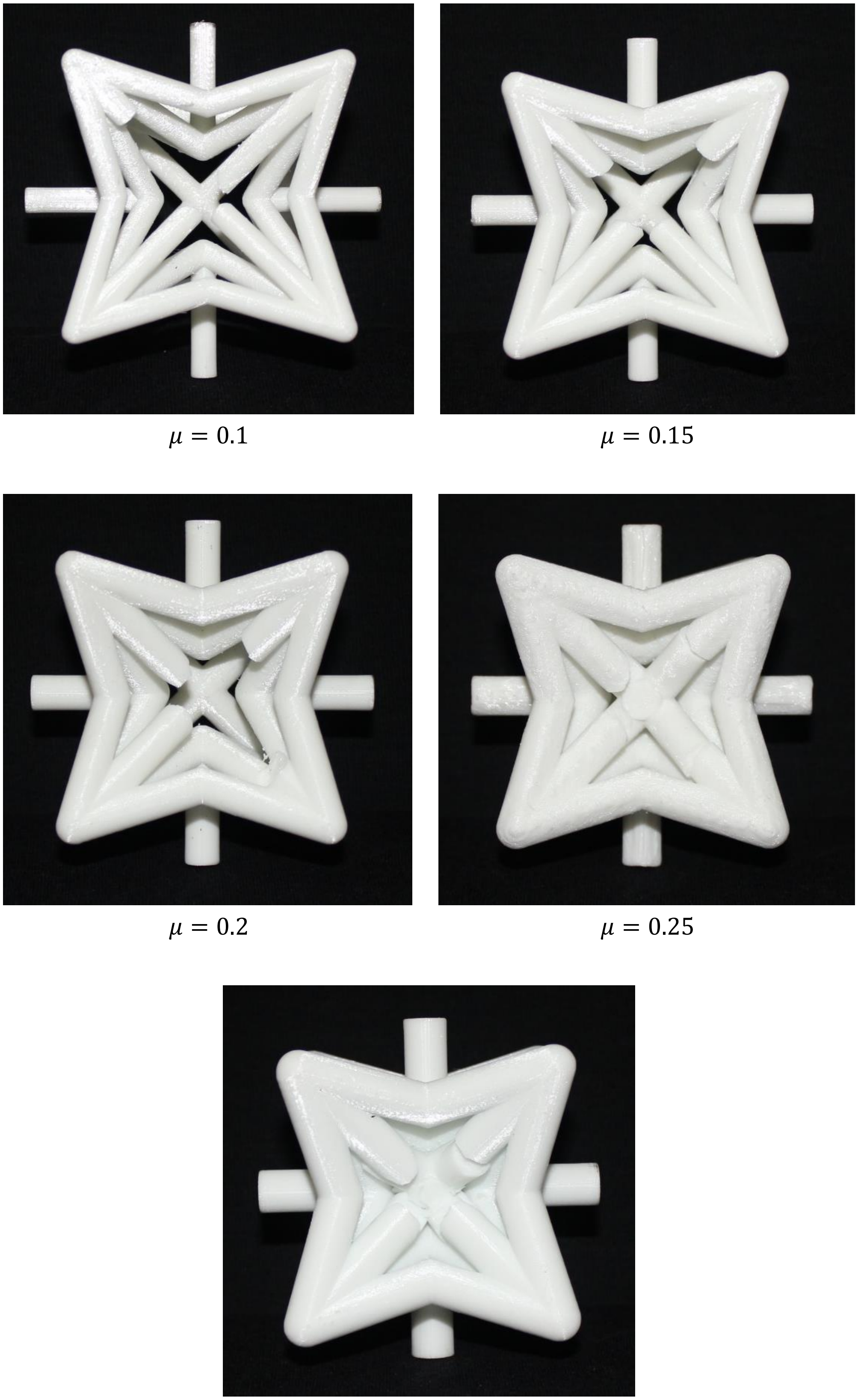

$\mu = 0.1$ $\mu = 0.15$

$\mu = 0.2$ $\mu = 0.25$

$\mu = 0.3$

Figure 10: Top view of specimens with different relative densities after final fracture

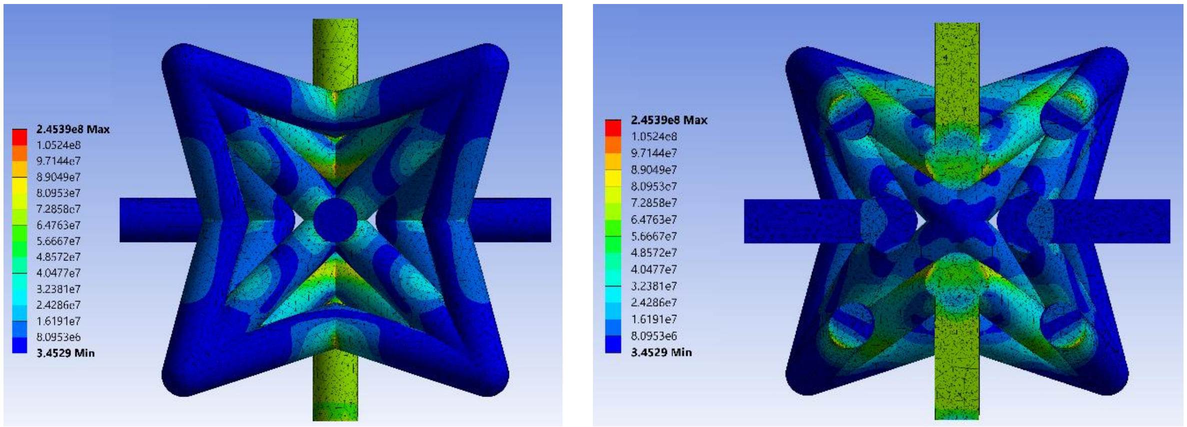

(a) (b)

Figure 11: Von Mises equivalent stress for FE model constructed by volumetric elements for $\boldsymbol{\mu} = \mathbf{0.2}$: (a) side view (b) middle-section view of the unit cell

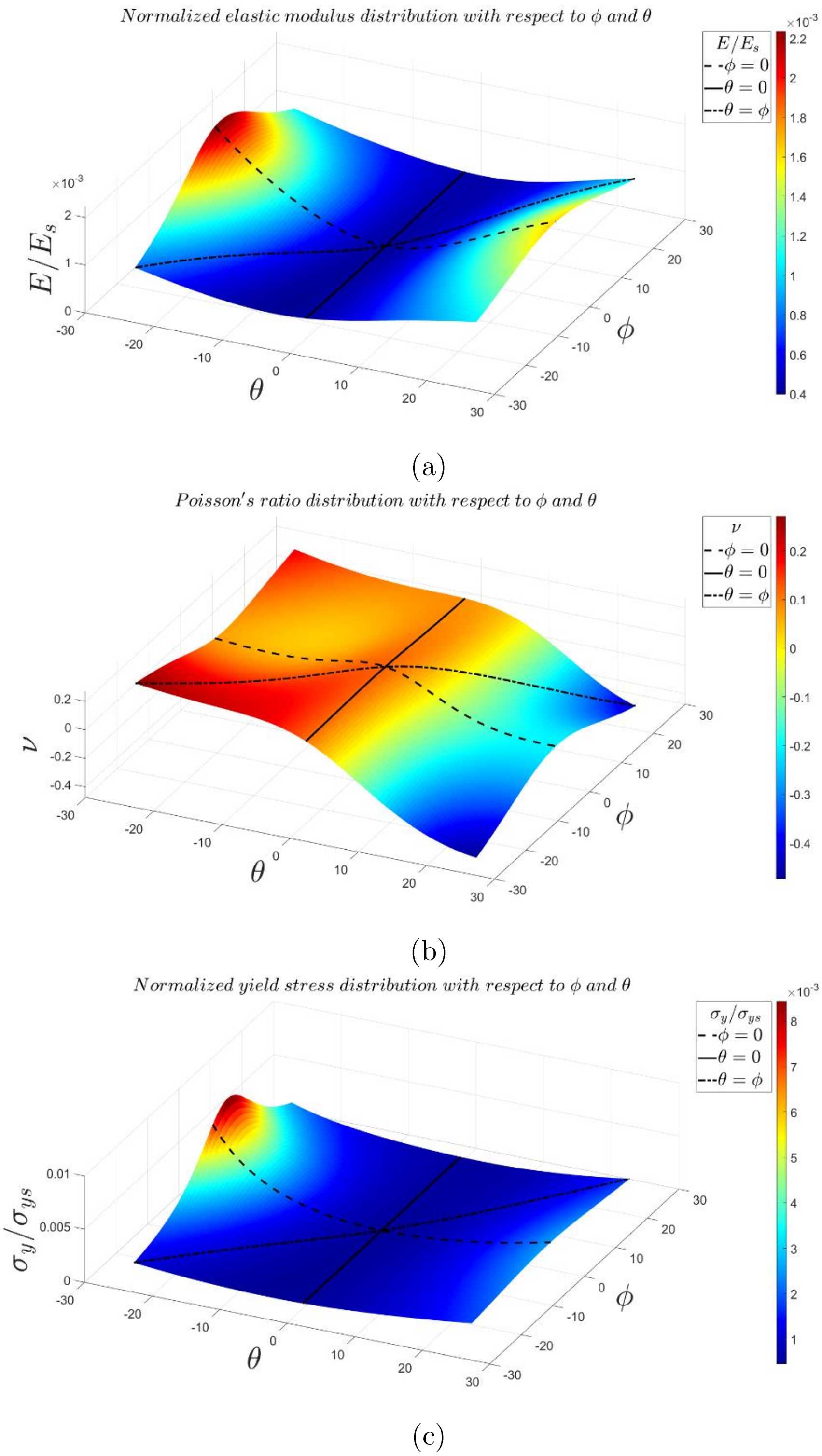

(a)

(b)

(c)

Figure 12: Variations of mechanical properties of general 3D re-entrant unit cell with respect to $\boldsymbol{\theta}$ and $\boldsymbol{\varphi}$ in $\boldsymbol{r_1 = r_2 = r_3 = 0.14b}$: (a) elastic modulus, (b) Poisson's ratio, and (c) yield stress. Specific cases such as $\boldsymbol{\theta = 0}$, $\boldsymbol{\varphi = 0}$ and $\boldsymbol{\theta = \varphi}$ have also been shown as lines

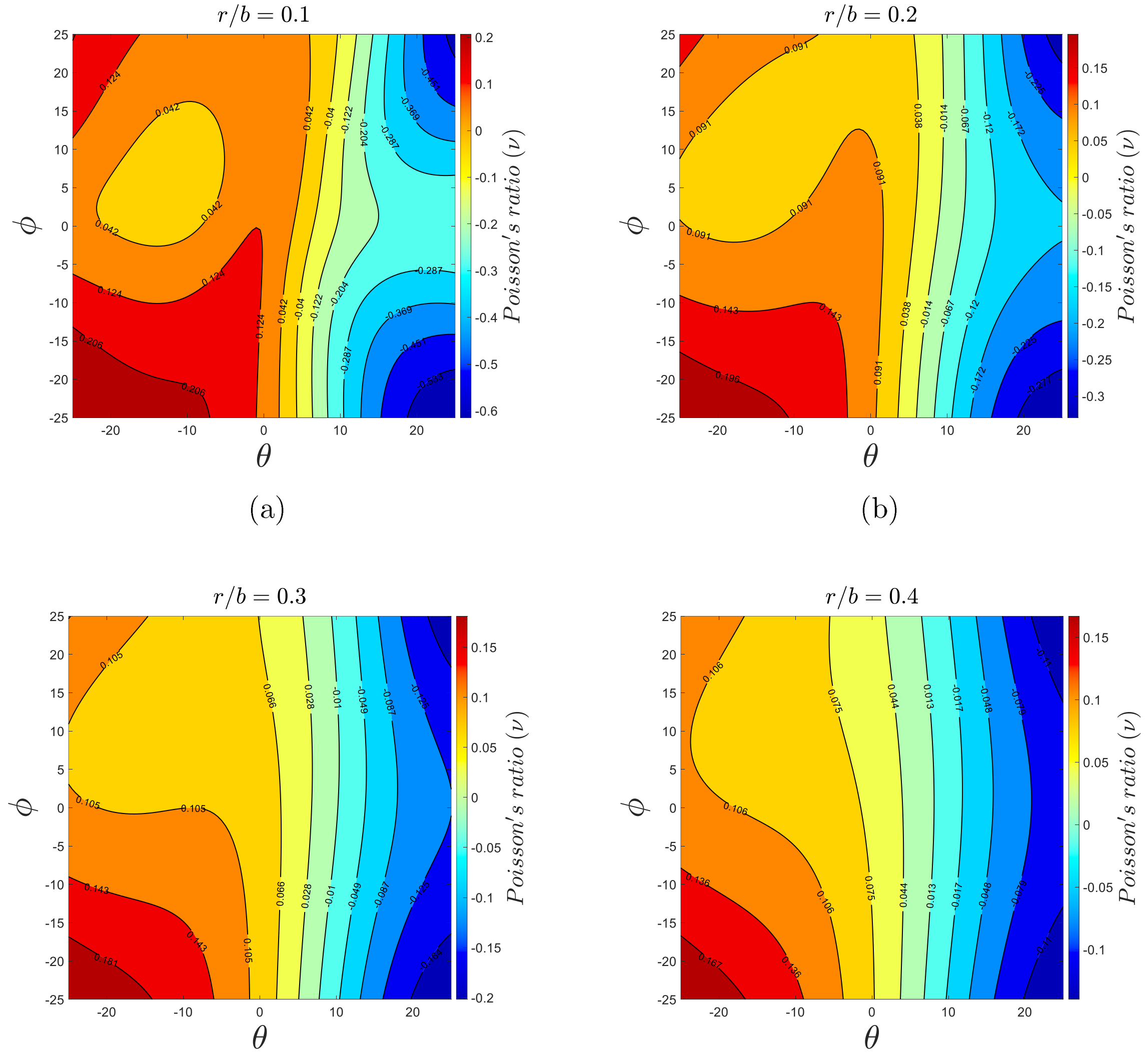

(a)

(b)

(c)

(d)

Figure 13: Variations of Poisson's ratio with respect to θ and φ: (a) $r/b = 0.1$, (b) $r/b = 0.2$, (c) $r/b = 0.3$, and (d) $r/b = 0.4$.

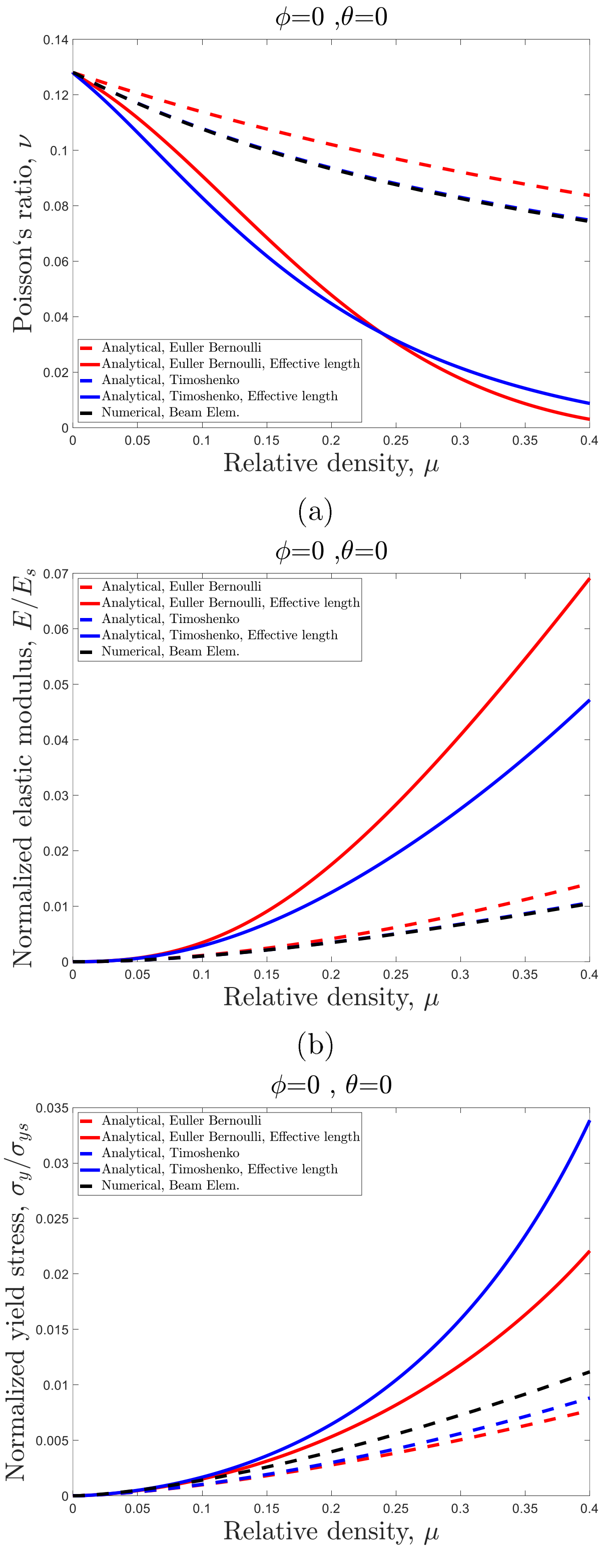

(a)

(b)

(c)

Figure 14: Mechanical properties variations of structure with $\boldsymbol{\varphi = 0}$, $\boldsymbol{\theta = 0}$: (a) elastic modulus, (b) Poisson's ratio, and (c) yield stress

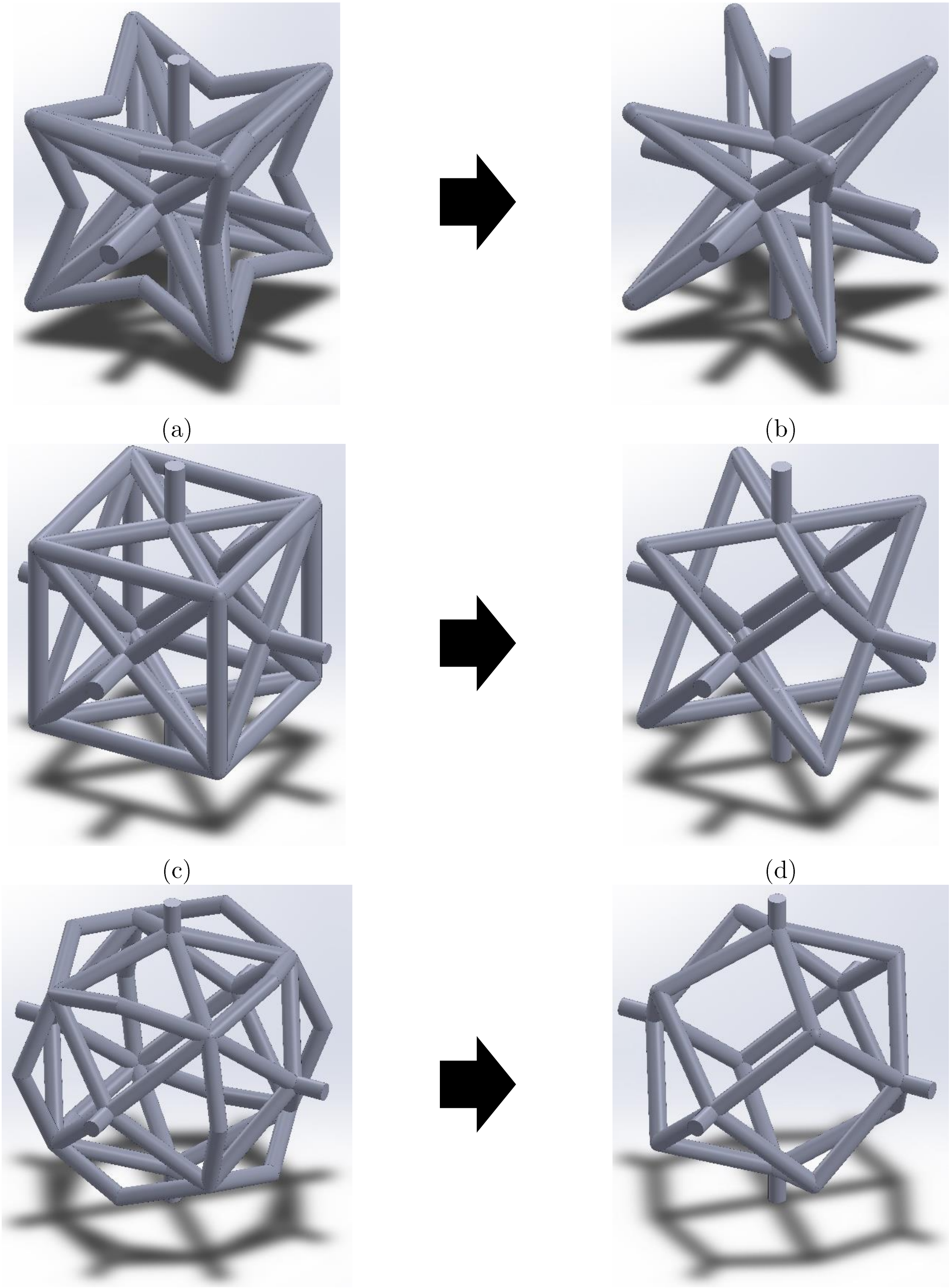

(a) (b)

(c) (d)

(e) (f)

Figure 15: Generic geometry of the unit cell with positive (top), zero (middle), and negative (bottom) values of $\boldsymbol{\theta}$ ***and*** $\boldsymbol{\varphi}$ ***for general unit cell (left column) and lightened unit cell (right column)***

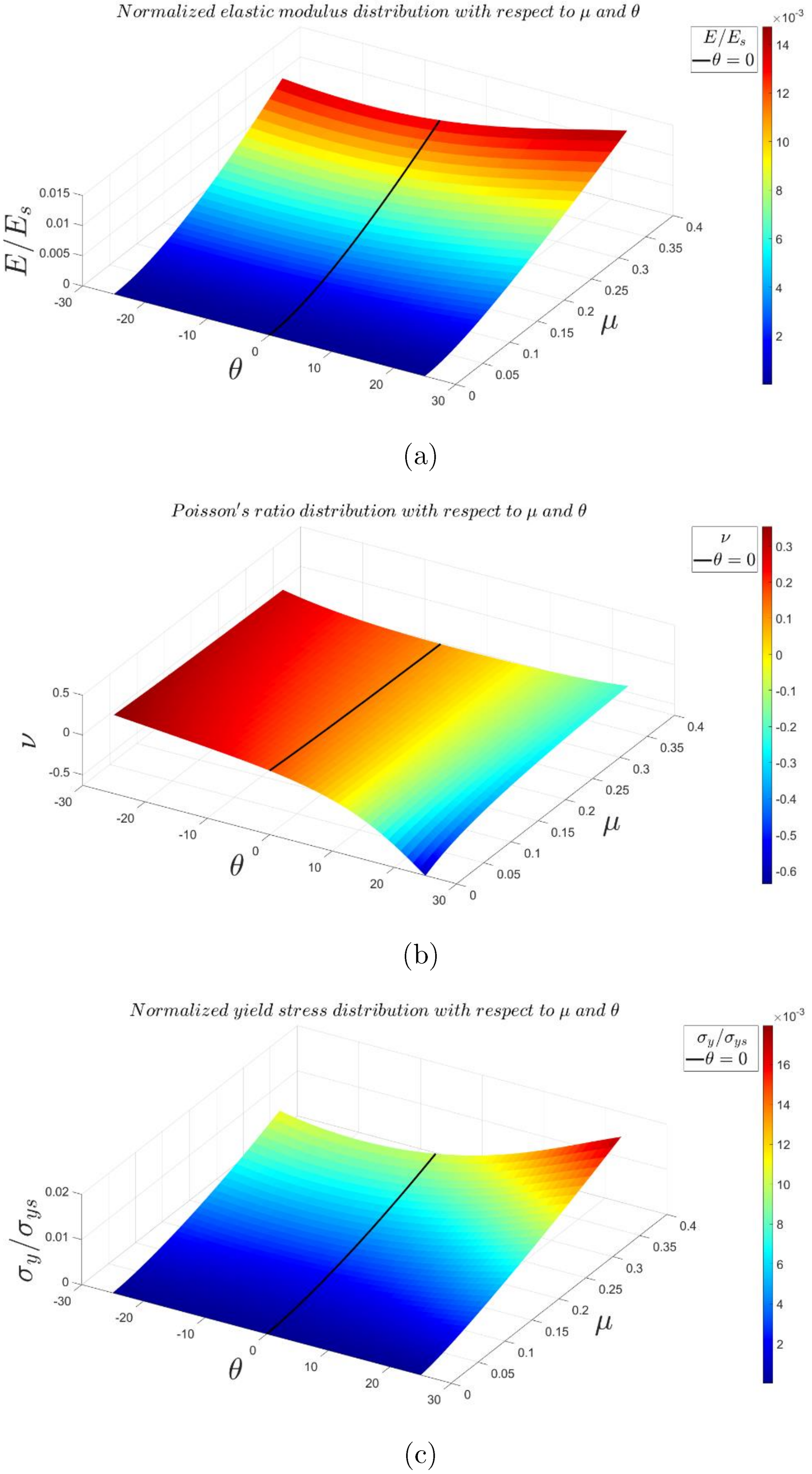

Figure 16: Variations of mechanical properties of lightened structure with respect to $\boldsymbol{\theta}$ and $\boldsymbol{\mu}$: (a) elastic modulus, (b) Poisson's ratio, and (c) yield stress. The specific case of $\boldsymbol{\theta} = \mathbf{0}$ is shown as solid line

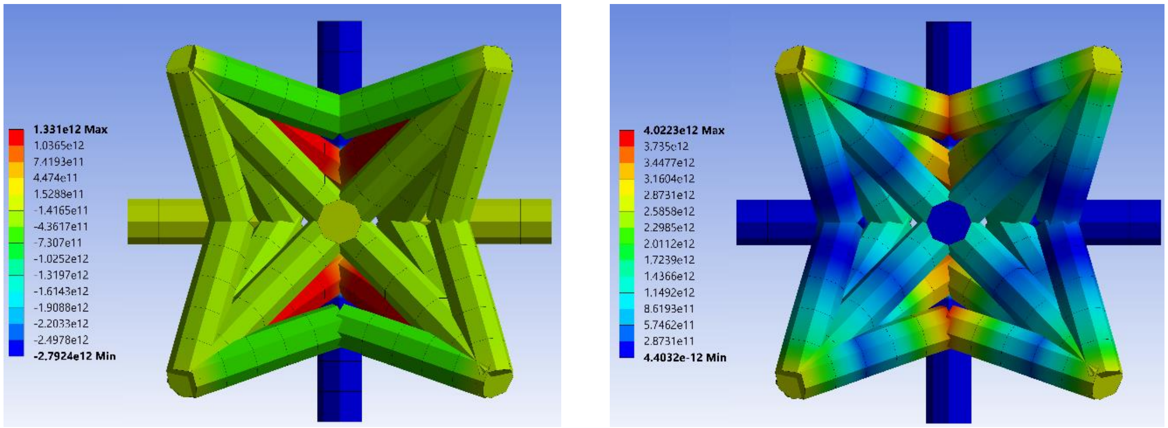

(a) (b)

Figure 17: Stress distribution of FE model constructed by Beam 189 elements for $\boldsymbol{\mu = 0.2}$: (a) normal stress (b) flexural stress